8-2017

Joule Heating Enabled Electrokinetic Trapping of Submicron Particles in Ratchet Microchannels Using Depth Modelling

Abhinav Kalkhanda
Clemson University, abhinavkalkhanday@gmail.com

JOULE HEATING ENABLED ELECTROKINETIC TRAPPING OF SUBMICRON PARTICLES IN RATCHET MICROCHANNELS USING DEPTH MODELLING

A Thesis

Presented to

the Graduate School of

Clemson University

In Partial Fulfillment

of the Requirements for the Degree

Master of Science

Mechanical Engineering

---

by

Abhinav Kalkhanda

August 2017

Accepted by:

Dr. Xiangchun Xuan, Committee Chair

Dr. Xin Zhao

Dr. Ethan Kung

ABSTRACT

Microfluidic devices have been increasingly used for diverse particle manipulations in various chemical and biological applications. Fields such as water quality control, environmental monitoring and food safety require the continuous trapping and concentration of particles (either bio- or non-bio) for enhanced detection and analysis. To achieve this, various microfluidic techniques have been developed using electric field as well as other fields including magnetic, optical, acoustic, hydrodynamic, gravitational and inertial. Among these methods, electrokinetic manipulation of particles is the most often used due to its advantages over other methods such as simple operation and easy integration etc. It transports fluids and controls the motion of the suspended particles via electroosmosis, electrophoresis and dielectrophoresis. However, there is an inevitable phenomenon accompanying electrokinetic devices, i.e., Joule heating due to the passage of electric current through the conductive suspending medium. Previous studies indicate a negative impact of Joule heating on the trapping and concentration of micron-sized particles in insulator-based dielectrophoretic microdevices. We demonstrate in this thesis that the Joule heating-induced electrothermal flow can actually enhance the electrokinetic manipulation, leading to the otherwise impossible trapping and concentration of submicron particles in ratchet microchannels.

We fabricated ratchet microchannels with polydimethylsiloxane and used them to study the transport and control of submicron particles in a moderately conductive phosphate buffer solution. Our research group did the experiments previously. We

developed a numerical multiphysics depth average model, which can predict the observed particle trapping in the ratchet region. The numerical model consists of coupled electric current, fluid flow, heat transfer and mass transport equation. A depth average analysis of these governing equations was done to develop a 2D model on the horizontal plane of the microchannel, which gives us numerical results that are as good as a full-scale 3D model developed previously, but with much less computational resources. Numerical analysis of the developed model predicts the formation of two counter rotating electrothermal vortices at the ratchet tips. Moreover, particles can be seen trapped inside these vortices and the concentration of particles trapped in electrothermal vortices can be observed to increase with time. Further, on doing the parametric study we found out that with increase in voltage the size of these vortices increases. We also changed the shape of the ratchet, but that does not seem to affect particle trapping in a significant manner. These obtained numerically predicted results are found to be in good agreement with our experimental observations, which further validates our numerical modelling.

DEDICATION

I dedicate my thesis to my parents who always encouraged me to work harder and gave me their support at all times. I thank my friends both here in USA and India who always believed in me and helped me in all way possible.

ACKNOWLEDGMENTS

I would like to thank my research advisor, Dr. Xiangchun Xuan for giving me this great opportunity to work with him and providing me his valuable inputs throughout this research work. His thoughts and constant motivation helped me a lot during my work. I learned a lot about professional work environment, which will help me a lot in my future professional job. I would also like to thank my committee members Dr. Ethan Kung and Dr. Xin Zhao for their valuable inputs. I would also like to thanks mechanical engineering department for assistantship, which helped with my expenses.

I would also like to thank my fellow research group students Rama, Akshay, Di and Yilong for providing their valuable inputs, which helped in successfully completing my thesis work. I would also like to thank my friends in Clemson who made my life at Clemson enjoyable and motivated me to work harder. I would also thank my friends in India and USA who always supported and motivated me in spite of the distance.

I am very grateful to my family for supporting me throughout in all ways possible and always believing in me.

TABLE OF CONTENTS

Page

Table of Contents (Continued)

Page

LIST OF TABLES

Table Page

LIST OF FIGURES

List of Figures (Continued)

Figure Page

List of Figures (Continued)

Figure Page

List of Figures (Continued)

Figure Page

CHAPTER ONE

INTRODUCTION

1.1 Motivation

Microfluidics as the name suggests deals with the behavior of fluids on a sub-millimeter scale [1]. It is being used in different areas such as DNA chips, inkjet printheads, Lab-on-a-chip device, molecular biology, optics, acoustic droplet ejection and fuel cells. LOC or Micro total analysis system is a device, which has a chip of size millimeters to few square centimeters and can be used to integrate single or multiple circuits on it [2], has low fabrication cost [3], faster analysis and response time, better control of process, massive parallelization allows tens or hundreds of operations to be performed simultaneously on a chip [4] and automatic verification of parts quality [5]. Because of the increasing demand for cheap and faster manufacturing of chips, new technologies such as polydimethylsiloxane (PDMS), ceramic, glass, metal itching, OSTE polymer processing, deposition, and bonding have been developed. PDMS material is inexpensive, optically transparent, flexible, and can be easily fabricated and bonded on other surfaces. Due to these advantages, it is preferred over silicon and glass materials [6].

LOC devices have the ability to effectively and accurately manipulate particles on micro scale. Various ways in which samples are manipulated include focusing, filtering, mixing and trapping. Research fields such as food safety, water quality control and environmental monitoring require concentration and trapping of particles in a continuous flow to detect and analyze particles [7, 8]. To achieve this kind of manipulation, different sources by which force field can be generated such as electrokinetics [9, 11], magnetic [12,

13], inertial [14], optical [15, 16], acoustic [17, 18], and hydrodynamic [19-21] are used. Another technique used to trap and manipulate particles include contactless and surface contact methods. Contactless method is preferred over surface contact method because it helps to achieve reversible and flexible trapping. Electrokinetics having advantages such as simple operation, easy integration, and small dispersion of sample is an efficient and preferred means for particle manipulation. It transports fluids and controls the motion of suspended particles via electroosmosis, electrophoresis and dielectrophoresis. The electrokinetic phenomenon has been studied in a variety of microchannel shapes such as straight, curved or network of channels [22-24]. Even though it has many advantages, it severely suffers from the inevitable effect of Joule heating. Due to Joule heating, the temperature rises in the microfluidic device and this rise in temperature is seen to adversely affect the fluid flow and particle manipulation [25-27]. When Joule heating is negligible, this method has been used to manipulate particle and cells [28-31] using dielectrophoresis. In this work, we demonstrate that joule heating can be exploited to enhance electrokinetic manipulation and trapping using electrothermal flows, leading to trapping and concentration of sub-micron particles in a ratchet microchannel.

The electric field is amplified on passing through a constriction region, which is a ratchet channel is our work. This amplified electric field raises the temperature of fluid and causes gradients in temperature dependent properties giving rise to joule heating. Electrothermal flows are generated due to this joule heating which can be exploited to trap and concentrate particles. This thesis attempts to give a detailed experimental and numerical explanations of these phenomenon. To develop better understanding of the

above discussed phenomenon, in the next section we will discuss about background of electrokinetics.

1.2 Background

Electrokinetics is the phenomenon that takes place in a microfluidic system when an electric field is applied to the system. An external voltage is applied across the channel, which generates an electric field and is used to pump the fluid in the channel and manipulate sample motion. In a pressure driven flow, the velocity profile is parabolic in nature, which causes sample dispersion due to velocity gradients. However, in electrokinetic flow, the flow is plug like across the channel and has a constant value of velocity throughout. Due to this, the concentration of the sample is uniform throughout the entire flow field and hence the dispersion, which occurs due to a non-uniform field, is minimized. This section provides background information about the different effects that are present in electrokinetics. The information provided here is taken from various textbooks on microfluidics [37-43] and readers may refer to them for even better understanding.

1.2.A The Electric double layer (EDL)

Electrical double layer or EDL is considered as the basis of the electrokinetic phenomenon in a microchannel. In the microchannel, we a have a solid-liquid interface. The electrical double layer is present near this interface, which has a non-zero charge density of ions. Various mechanisms such as charged crystal surfaces, isomorphic substitutions of charged groups, ionization of surface groups and specific absorption of

ions [44] are responsible for the charge that is acquired on the solid surface of the microchannel. Electrolyte solution that is present in the microchannel is initially neutral in charge. When this solution is exposed to the solid surface, the solution near the wall acquires the charge opposite to that of solid surface. Therefore, the concentration of counter ions i.e. opposite charge ions increases near the wall. The co-ions are repelled into the bulk of the fluid where an electro neutrality is maintained. Due to this process, the electrical double layer is developed near the wall. The net charge density decreases to zero from EDL to the bulk of fluid [45]. Inside the electrical double layer, the presence of opposite charges creates an electric potential along the width of EDL. Figure 1 can illustrate the above charge distribution.

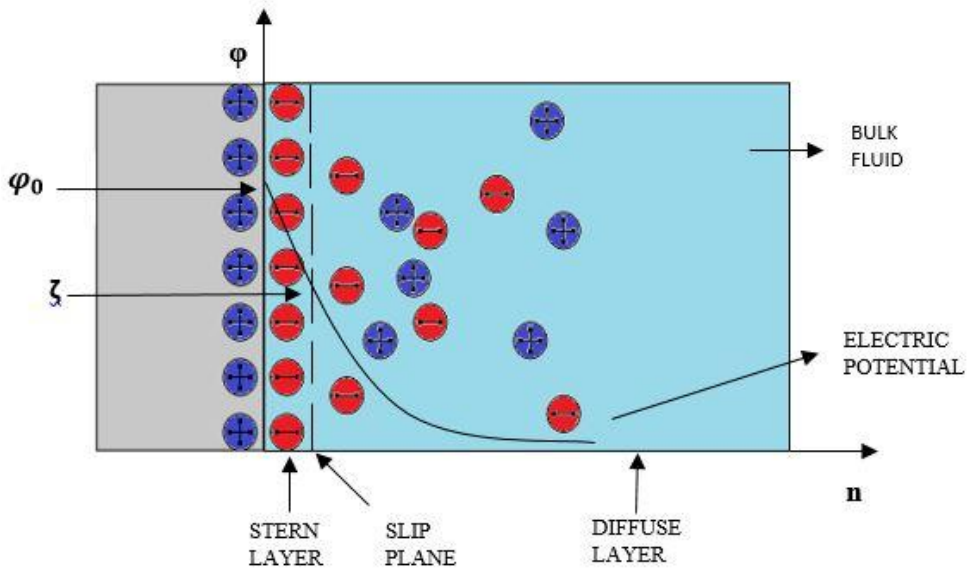

Figure 1.1 Representation of electrical double layer near the wall. The distribution of co-ions and counter-ions near the stern layer and diffuse layer is shown. The zeta potential at the slip plane is highlighted. The electric potential is plotted as a function of direction "n" which is normal to the solid wall.

Two regions are defined based on above knowledge namely Stern layer and diffuse layer. The stern layer is the layer, which is very close to the wall and is of the order of two times the diameter of counter ions. Across the stern layer, the electric potential drops linearly [46]. In the diffuse layer, which is present outside the stern layer the motion of ions takes place due to diffusive repulsion and electrostatic attraction. A slip plane separates these two regions.

1.2.B Electroosmosis

When an external electric field is applied across the channel, it causes the electrolyte to move in a direction, which is tangential to the charged surface. This motion is termed as Electroosmotic flow. The electrical double layer has net non-zero charge density; therefore, it experiences a net force. This force induces a motion within the electrical double layer and therefore causes the motion in the bulk of the fluid due to the viscous drag. The Navier-Stokes equation can be integrated over the electrical double layer using the body force term. The body force term is defined as $\rho_e \mathrm{E}$. The mathematical process can be referred at [47]. The Velocity profile inside the electrical double layer is given by

$$u(n) = -\frac{\varepsilon}{\eta}(\varphi(n) - \zeta_w)\mathrm{E} \tag{1.B.1}$$

Where $u(n)$ is the velocity distribution in the direction "n" which is normal and away from the solid wall, ε is the electrical permittivity of fluid [F/m], η is the viscosity of fluid [Pa·s], $\varphi(n)$ is the electric field distribution in the direction "n" which is normal and away from the solid wall, ζ_w is the equilibrium wall zeta potential [V] and E is the applied

electric field. The no-slip boundary condition is satisfied at the wall. In the bulk of the fluid, the fluid velocity is like a plug like profile and is given by

$$u_{eo} = -\frac{\varepsilon}{\eta}\zeta_w E \tag{1.B.2}$$

$$\mu_{eo} = -\frac{\varepsilon}{\eta}\zeta_w \tag{1.B.3}$$

μ_{eo} is the electroosmotic mobility [m^2V/s].

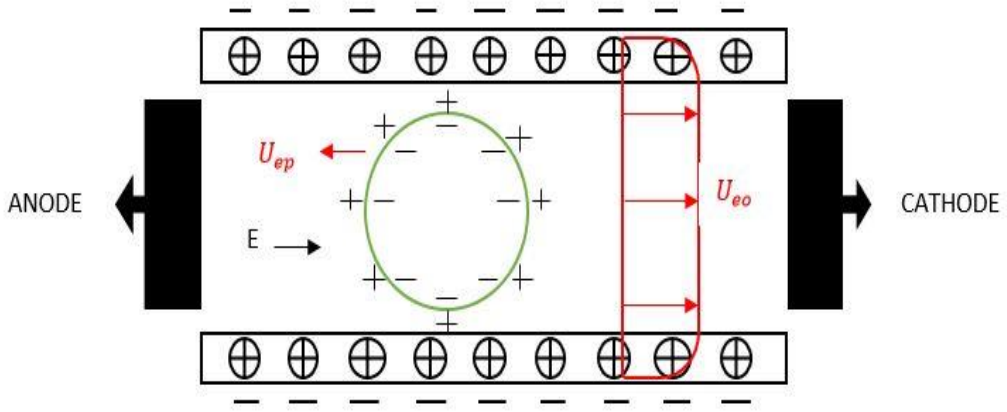

Figure 1.2. Schematic representation of electroosmotic velocity profile inside a microchannel. This flow profile is induced due to Coulomb force on the electrical double layer. Velocity variation occurs inside the electrical double layer and outside the EDL it is plug-like flow.

1.2.C Electrophoresis

When external electric field is applied, it causes the motion of charged ions with respect to suspending medium and is termed as electrophoresis. This thesis deals with the manipulation of particles, which get charged when suspending in a fluid. The electrophoresis due to surface charge is discussed here. The surface of the particle gets

charge in a similar manner as the solid wall. The electrical double layer is formed on the surface of the particle. The fluid inside the electrical double layer moves due to the applied external electric field. If we assume that the bulk fluid is stationary, then the particles relative motion would be in the opposite direction. Electrophoresis has been extensively exploited for manipulation of species and particles [48-84]. Under applied electric field these particles experience an opposite directing Coulomb force as compared to Electroosmosis; therefore Electroosmosis and electrophoresis are opposite in direction to each other. The electrophoretic velocity (EP) of the particle, Uep is given by the following equation

$$u_{ep} = \mu_{ep} E \tag{1.C.1}$$

$$\mu_{ep} = \frac{\varepsilon}{\eta} \zeta_p \tag{1.C.2}$$

μ_{ep} is the electrophoretic mobility, ε is the electrical permittivity of fluid [F/m], η is the viscosity of fluid [Pa·s], ζ_p is the particle zeta potential [V] and E is the applied electric field. Electrokinetic velocity u_{ek} is given by the vector sum of electroosmotic and electrophoretic velocity.

$$u_{ek} = \mu_{ek} E \tag{1.C.3}$$

$$\mu_{ek} = \frac{\varepsilon}{\eta} \left(\zeta_p - \zeta_w \right) \tag{1.C.4}$$

μ_{ek} is the electrokinetic mobility, ε is the electrical permittivity of fluid [F/m], η is the viscosity of fluid [Pa·s], ζ_p is the particle zeta potential [V], ζ_w is the equilibrium wall zeta potential [V] and E is the applied electric field.

1.2.D Dielectrophoresis

When an electric field is applied the polarizable species (charged or uncharged), experience a force due to non-uniformities in the electric field which is called as dielectrophoretic force Pohl [85, 86]. Both reservoir based dielectrophoresis and insulator-based dielectrophoresis can be used for manipulation, trapping and sorting of particles [87-90]. The DEP is given by the expression

$$\mathrm{F}_{DEP} = \frac{\pi}{4}\varepsilon a^3 f_{CM} \nabla |\mathrm{E}|^2 \tag{1.D.1}$$

The DEP force that acts on the particle depends on the strength of electric field, properties, the size of particle and frequency of AC electric field.

When no Electroosmosis and electrophoresis is present the particle will move due to this force and the velocity of the particle can be calculated using Stokes drag relation.

$$\mathrm{U}_{DEP} = \frac{\varepsilon a^2}{12\eta} f_{CM} \nabla |\mathrm{E}|^2 \tag{1.D.2}$$

$$f_{CM} = \left(\sigma_p - \sigma_f\right)/\left(\sigma_p + 2\sigma_f\right) \tag{1.D.3}$$

Where f_{CM} is the Clausius-Mossotti factor, a is the diameter of the particle, ε is the electrical permittivity of fluid [F/m], η is the viscosity of fluid [Pa·s], σ_p and σ_f are the electrical conductivity of particle and electrolyte solution respectively.

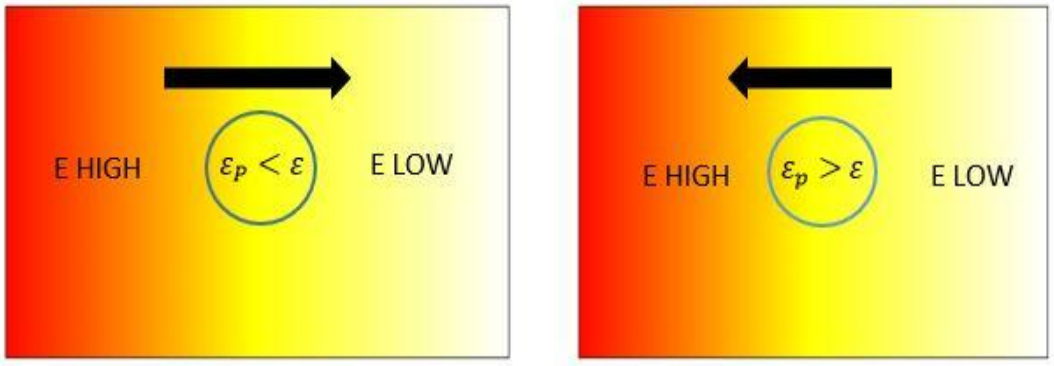

a **b**

Figure 1.3 Diagram shows dielectrophoresis of a spherical particle under the influence of non-uniform electric field. **(a)** If the particle is more polarized than the fluid, it moves from low electric field to high electric field. **(b)** If the particle is less polarized than the fluid, it moves from high electric field to low electric field.

If the Clausius-Mossotti factor is positive i.e. ($\sigma_p > \sigma_f$), particle is more polarized than the fluid, the particle will move from lower electric field region to higher electric field region. This is called as positive dep. If the Clausius-Mossotti factor is negative i.e. ($\sigma_p < \sigma_f$), particle is less polarized than the fluid, the particle will move from higher electric field region to lower electric field region. This is called as negative dep. The summation of fluid velocity, EP velocity, and DEP velocity gives us the total velocity of the particle. It is expressed by the following equation.

$$\mathrm{U}_P = \mathrm{u} + \mathrm{u}_{ep} + \mathrm{U}_{DEP} \qquad (1.D.4)$$

1.2.E Joule Heating

When an electric current passes through a medium, it is converted into heat energy due to resistance and is known as Joule heating. When an electric field is applied along the microchannel, it passes through the electrolyte solution, which leads to resistive heating. This Joule heating can be observed in all of the electrokinetic phenomena. Electric current is defined as a function of electric field, electrical conductivity and the area of the microchannel. If we consider a channel of length L, Width W and depth D, electric field E and electrical conductivity σ then electric current I is mathematically represented as

$$I = \frac{WH\sigma\Delta V}{L} \tag{1.E.1}$$

$$E = \frac{\Delta V}{L} \tag{1.E.2}$$

Therefore, volumetric rate of Joule heat generation can be represented a

$$Q''' = \sigma \frac{\Delta V^2}{L^2} = \sigma E^2 \tag{1.E.3}$$

The temperature rise inside the domain is due to the above-shown heat generation term. The rise in temperature causes a gradient in temperature field and hence we see the change in temperature dependent fluid properties [91, 92]. Since the microchannel geometry that we use is ratchet, the heating inside channel is non-uniform, due to which we have a non-zero value of electrothermal body force. As a result revolving patterns are formed which is known as electrothermal flow [93].

$$f = \rho_e \mathrm{E} - 0.5\mathrm{E}^2\nabla\varepsilon \tag{1.E.4}$$

Where, ρ_e is the volume charge density in C/m^3, E is the applied electric field in V/m and ε is the permittivity of the fluid.

1.3 Thesis Structure

After the completion of chapter 1, which gives us idea and basic concepts relevant to this thesis work, there are five more chapters included in this thesis. In Chapter 2, we discuss in details the experimental procedure carried around in the laboratory. In this chapter, we also discuss different material properties because they play a major role when we discuss joule heating and particle trapping. To validate our numerical model we compare them with the experimental results, so experimental procedure is taken into discussion. Chapter 3 discusses about the details of the governing equations that are used in the numerical modelling and corresponding boundary conditions involved. Since in this thesis work we have developed a 2D depth average model, which has advantages over 2D and 3D modelling. The 2D death model can predict the results with good accuracy and saves time and resources, which goes into 3D modelling. The fourth chapter includes the details of the experimentally obtained and numerical predicted results and their comparison. The effect of joule heating on different parameters and trapping of sub-micron particles in the vortices in the channel region. Chapter 5 involves the parametric study of the experimental and numerical models. Shape of the ratchet geometry is altered and the results are discussed. The parametric effect of changing the depth of channel is also taken into account. In the final chapter, we summarize about chapter two, three, four and five conclusion respectively and attempt to discuss about the direction of future work

Chapter 2

Experimental Methods and Setup

2.1 Introduction

This chapter gives us insight about the various experimental procedure that is used during the experimental work [97]. The experimental procedure involves fabrication of microchannel, fabrication of microdevices, the experimental procedure used. Details about the material properties also include since they have a key importance in our experimental as well as numerical modeling. A brief introduction about the computational detail is given at the end of the chapter to help better relate our numerical model with the experimental setup.

2.2 Microchannel Fabrication

A standard soft lithography technique is used for the fabrication of the microchannel. The ratchet used in this work is fabricated in polydimethylsiloxane (PDMS). The details of the 25μm microchannel (which is used for modeling) is explained below.

The glass slides that we use are of 1mm thickness. They are initially stored in acetone solution (Fischer Scientific) for about 3 hours. After that, an ultrasonic cleaner (Branson 2510) is for about 5 min to rinse the glass slides. De-ionized water (Ricca Chemical Company LLC, Arlington TX) is then used to dry the glass slides. Nitrogen gas is used to dry the glass slides. Furthermore, the glass slides are heated (HP-30 A, Torrey Pines Scientific) for about 10 minutes at 120 degree Celsius to ensure complete drying. To obtain even better finish of the glass slides, they are plasma treated (PDC-32G, Harrick Scientific) for 1 minute.

The glass slides are coated with a film of SU-8-25 photoresist (Microchem). Spin coated (WS-400B-6npp/lite, laurel technologies) is used for coating the slides. The spin coater is ramped from 1000 rpm for 5 sec to further 300rpm for 5 sec to a terminal speed of 2000rpm. It is kept at this speed for 25 sec to generate the film. A 2D-Sketch of the channel made from CAD model and is placed over the slide. The films are then exposed to UV light (ABM Inc. San Jose, LA) for 30 sec. The previously mentioned process of baking the films for 1 minute and 3 minute and their treatment with SU-8 developer solution (Microchem) for 4 minutes is done again. Isopropyl alcohol solution (Fisher Scientific) is used for rinsing. A final baking is done at 65 degree Celsius for 1 minute and 15 degree Celsius for 5 minutes to develop molds over the slides.

For the preparation of PDMS, we need curing agent (Sylguard 184 silicone elastomer) and polymer base in the ratio 1:10. The mixture is de-grassed (13-262-280 A, Fisher Scientific) at a vacuum of 20Psi for 20 min. It is then poured over the mold to obtain a thickness of two mm. Baking is done at 70 degree Celsius for two hours in a gravity convection over (13-246-506GA, Fischer Scientific) to generate hardened PDMS with the desired 25μm uniform depth.

2.3 Microdevice Fabrication

A scalpel is used to cut PDMS which has master microchannel cavities from the Petri dishes. A 5 mm diameter punch is used to cut cylindrical reservoirs over the predefined circular extensions of 6 mm diameter. A nitrogen jet is used to completely clean the cavities. A plasma treatment is done for 2 minutes so that the PDMS is permanently bonded over the glass slides. A final form of the developed microdevice is illustrated in figure 2.1

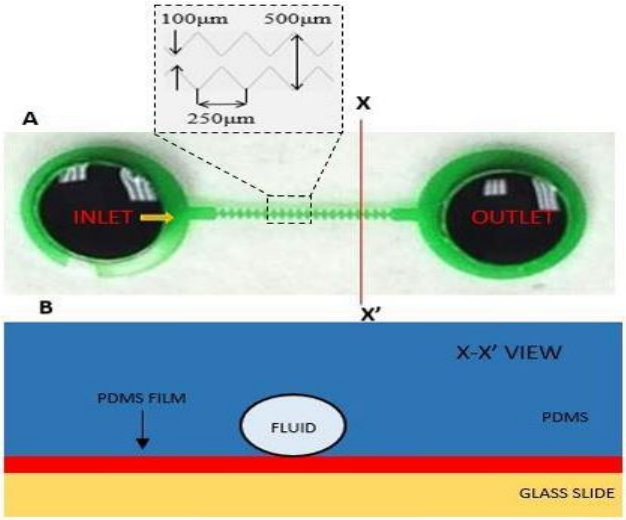

Figure 2.1 The diagram A shows the top view of the experimental setup of the microchannel geometry with an enlarged image of the ratchet channel. Diagram B shows the cross-sectional view of the microchannel used in the experiment. The arrow shows the direction of the electroosmotic flow.

2.4 Experimental Method

The working fluid consists of buffer solution and polystyrene microsphere. The buffer solution is prepared as per the required concentration. To ensure uniform wetting, the microdevice is filled with pure buffer and left for 10 minutes. This also helps in maintaining the hydrophilic surface of the walls and a uniform wall zeta potential. To ensure we have uniform concentration throughout the microchannel, a high-speed vortex (Fischer Scientific) is used before starting the experiment. Working fluid is then filled in the channel. Since we have no pressure driven flow in our model, the level of the working fluid is closely maintained at the same level in the reservoir.

In this research work, we use DC-biased AC voltage across the channel. The DC voltage is kept fixed at 50V DC while the AC Voltage is varied. The AC voltage has a frequency of 1 KHZ. The DC voltage is responsible for driving the electroosmotic flow. When AC voltage increases, it is responsible for increasing the Joule heating and potential across the microchannel to manipulate particle motion.

As mentioned before, we apply the voltages across the microchannel to develop a potential drop and drive the working fluid across the microchannel. Two platinum electrodes are placed in the respective reservoir. The electrodes are 0.5mm in diameter. The applied voltage is generated by using a power supply (TREK, 609E-6) and a function generator (Agilent Technologies, 3320A). In this work, the particles that we use are sub-micron particles. To ensure good visibility of particles, a high-intensity fluorescent lamp (Nikon Intensilight C-HGHI). Since our aim is to develop a numerical model good enough to compare with our experimental work, we use a CCD camera (Nikon DS-QI1MC) to generate good quality video recordings of the performed experiment. We need to make sure that the frame rate (fps) and exposure time (ms) are appropriate. Nikon software (NIS-element AR 2.30) is used to generate images from the videos of experiments. We generate images of the concentration patterns at different times of the experimental videos and superimposition technique to generate images of streamlines inside the microchannel.

2.5 Wall and Particle Zeta potential calculation

The wall zeta potential is measured by performing an experiment consisting of two different kinds of solution. One solution is the solution if interest, while the other is a dilute solution, prepared by diluting the working fluid so that the electrical conductivity is within 95 percent of the original values. A straight microchannel is used for the experimental purpose which has two reservoirs at the opposite ends. One reservoir is filled with dilute solution and is allowed to go into microchannel by the capillary action. The other solution i.e. the solution of interest is immediately filled into another reservoir until both reservoirs attain the same level. This makes sure that there is pressure driven flow. The low DC electric field is applied to ensure that heating effect is minimum inside the channel. The DC voltage displaces the dilute solution from the microchannel. The obtained current values are then plotted against time and the graph between current and time is found to be linear. The slope of this graph gives us the value of the wall zeta potential. For the measurement of particle zeta potential, we introduce a particle in the microchannel. A low DC Voltage is applied as we did previously to avoid heating. The particle moves along the microchannel under the influence of electric field. The time taken particle to travel the distance is measure and speed of the particle are calculated from that. Using the electrokinetic mobility equation (1.C.4), the difference between the zeta potential and particle zeta potential is calculated. From the previous procedure, we already know the wall zeta potential. Therefore, particle zeta potential can be calculated from that. For more detailed mathematical and experimental procedure the readers may refer to Sze et al [94].

2.6 Computational Domain

After the experimental work is completed, the next step is to develop a numerical model good enough to give results, which can be compared to our experimental results. For performing the computational fluid dynamics, we use COMSOL 5.2a Multiphysics, a commercial finite element simulation software. We develop a 2D depth average model to study the effects of joule heating [95] and particle concentration in the microchannel region. This full-scale 2D Depth average simulation accounts for both the top and bottom sides of the channel and PDMS wall and includes additional terms for fluid flow and heat transfer in the standard governing equations, which is explained in detail in next chapter. These additional terms are not present in the 2D model, done previously by our research group [96]. Since top and bottom wall effects are not included in 2D model, they had to assume a very high value of heat transfer coefficient. This assumption is not required for this modeling. A full-scale 3D model was also developed by [97] for the ratchet channel. However, 3D model is quite expensive and requires a lot of computational time and resources for solving the model. This model neither require the assumption of high heat transfer coefficient since we have additional terms and does not require the use of supercomputer or Palmetto cluster for solving. For solving transient model, step size of 1 ms was taken. Meshing was done extremely fine for the constriction of ratchet tip region of microchannel. Appropriate mesh size was selected for obtaining grid independent solution. To reduce computational resources a nonlinear segregated iterative solver was used. The full-scale transient model can be solved using a laptop.

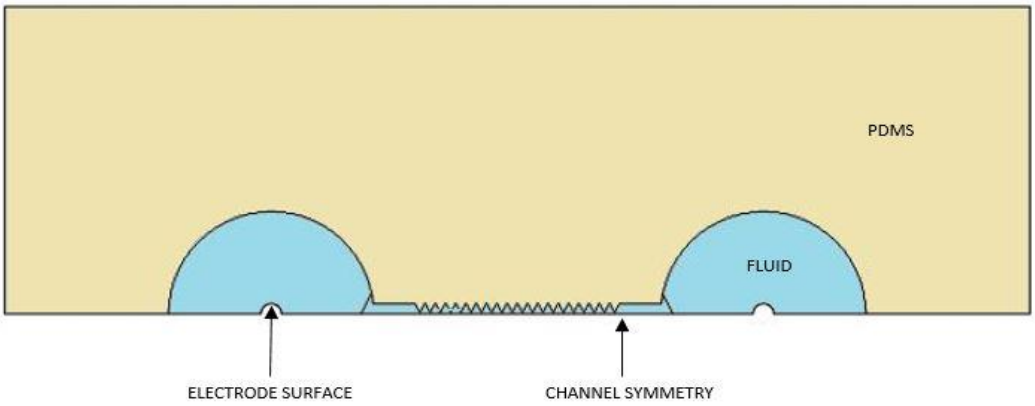

Figure 2.2 Schematic Representation of the 2D geometry drawn in COMSOL.

The 2D geometry is developed in the COMSOL software itself. A schematic diagram of the channel geometry is depicted in figure 2.2. We use only half of the geometry due to symmetric nature of the microchannel used in the experiment. In our numerical model the electric, heat transfer, flow field, and concentration equations are coupled. The electric, heat transfer, fluid flow, and concentration equation are solved for the microchannel region. Only heat transfer equation is solved for the PDMS region. In figure 2.2, we can see the electrodes are represented by two holes. The reason for that is, we use platinum electrodes, which have high electrical and thermal conductivity, so they are considered to remain at constant temperature and constant electric potential, and therefore we treat them as holes in our 2D numerical model. To apply above equations in COMSOL we have to use modules of electric current, creeping flow, heat transfer in fluids, heat transfer in solids and transportation of diluted species.

The fluid properties such as electrical conductivity, permittivity and viscosity are temperature dependent and are evaluated using the following expressions:

$$\sigma = \sigma_{\infty}[1 + \beta(T - T_{\infty})]$$

$$\varepsilon = \varepsilon_{\infty}[1 + \alpha(T - T_{\infty})]$$

$$\eta = 2.761 \times 10^{-6}\exp(1713/T)$$

Where σ_{∞} is the electric conductivity and ε_{∞} is permittivity of the fluid at room temperature T_{∞}, and α and β are their respective temperature coefficients. Other constants that are used in modeling and their respective values are given in the table below.

Table 2.1 Summary of the material properties and parameters that are used in modeling.

Symbol	Description	Value	Unit
k_{fluid}	Thermal conductivity of Fluid	0.61	W/(m·K)
k_{PDMS}	Thermal conductivity of PDMS	0.15	W/(m·K)
k_{glass}	Thermal conductivity of glass	1.38	W/(m·K)
$t_{us,PDMS}$	Thickness of PDMS slab	2	mm

$t_{ls,PDMS}$	Thickness of PDMS film	25	um
t_{glass}	Thickness of glass slide	1	mm
ζ_w	Zeta potential of walls	-45	mV
ζ_p	Zeta potential of particles	-65	mV
h	Natural convection coefficient	10	W/(m^2·K)
d_{ch}	Depth of microchannel	25	μm
α	Temperature coefficient of fluid electric permittivity	-0.0046	1/K
β	Temperature coefficient of fluid electric conductivity	0.02	1/K
σ_∞	Fluid electric conductivity at room temperature	0.5	S/m
ε_∞	Fluid electric permittivity at room temperature	8.854E-12	F/m
T_∞	Room Temperature	293	K

CHAPTER THREE

GOVERNING EQUATIONS AND BOUNDARY CONDITIONS.

3.1 Electric Field

The electric field is governed by the quasi-electrostatic equation [98]. Electric field equation is only solved for the fluid part of the equation since PDMS is considered as electrically insulating.

$$\nabla \cdot (\sigma E + i\omega D) = 0 \tag{3.A.1}$$

As mentioned before we use DC biased AC electric field in our experiment. The AC frequency, which is of order 1KHZ, is much less than the charge relaxation frequency $\sigma/2\pi\varepsilon$, which is of the order of MHZ [99]. Because of this, the electric field displacement has negligible effect. In the above equation, $E = -\nabla\phi$ is the electric field, ϕ is the electric potential, σ is the electric conductivity of the fluid, ω is the angular frequency and is given by $\omega = 2\pi f$, where f as the frequency. D is the electric field displacement and is given by $D = \varepsilon E$, where ε as the fluid's electric permittivity σE Which is the convection current has been assumed negligible as compared to conduction current [98].Based on above information the equation reduces to

$$\nabla \cdot (\sigma E) = 0 \tag{3.A.2}$$

We solve only for the DC component of the electric field, which is similar to our research group previous paper [96, 100, and 101]. As mentioned before we used 2D depth average modeling in this research work [95]. A depth average analysis of the above

equation (3.A.2) is done using an asymptotic method explained in Lin et al. [102]. The details of the derivation are as follows.

To perform the non-dimensional analysis following scales are used:

$[x, y] = H$, Length of the channel

$[z] = d$, Depth of the channel

[σ]= σ', Reference conductivity at room temperature

[ϕ]= ϕ' = E'H, E' is the reference electric field inside the channel

$[c] = c'$, Reference concentration

[T]=T', Room Temperature

$$[u, v] = U_{ev} = \frac{\varepsilon_\infty E' d^2}{\eta_\infty H}$$

$$[w] = U_{ev} \frac{d}{H}$$

$$\left[u_{ep,}\, v_{ep}\right] = U_{ep}$$

$$[w_{ep}] = \frac{U_{ep} H}{d}$$

$$[\eta] = \eta_\infty$$

$$[t] = t_0 = \frac{H}{U_{ev}}$$

∇_H Denotes the horizontal plane gradient i.e. along x and y-direction. The reference for the horizontal velocity is taken in such a way that body force term and viscous force terms are balanced. The continuity equation is used to calculate velocity along the z direction. The variable are expanded as:

$f = f_0 + \delta f_1 + \delta^2 f_2 + \cdots$ And so on

And the depth average function is defined as

$\bar{f} = \frac{1}{2}\int_{-1}^{1} f\, dz$

Using the above parameters equation (3.A.2) is non-dimensionalized as:

$$\delta^2 \nabla_H \cdot (\sigma \nabla_H \phi) + \frac{\partial}{\partial z}\left(\sigma \frac{\partial \phi}{\partial z}\right) = 0 \qquad (3.A.3)$$

δ^0 Order balance for (3.A.3) gives:

$$\frac{\partial}{\partial z}\left(\sigma_0 \frac{\partial \phi_0}{\partial z}\right) = 0 \qquad (3.A.4)$$

Considering $\sigma = \sigma(x, y)$ only we get

$$\frac{\partial}{\partial z}\left(\frac{\partial \phi_0}{\partial z}\right) = 0 \qquad (3.A.5)$$

Integrating and applying the insulating boundary condition on top and bottom surface gives us the equation

At z= ±1, $\left(\frac{\partial \phi_0}{\partial z}\right) = 0$

Hence $\left(\frac{\partial \phi_0}{\partial z}\right) = 0$ (3.A.6)

Therefore $\phi_0 = \phi_0(x, y)$ only.

δ^1 Order balance for (3.A.3) gives:

$$\frac{\partial}{\partial z}\left(\frac{\partial \phi_0}{\partial z}\right) = 0 \tag{3.A.7}$$

Integrating and applying the insulating boundary condition on top and bottom surface gives us the equation

$$\text{At z= } \pm 1, \left(\frac{\partial \phi_1}{\partial z}\right) = 0$$

$$\text{Hence } \left(\frac{\partial \phi_1}{\partial z}\right) = 0 \tag{3.A.8}$$

Therefore $\phi_1 = \phi_1(x, y)$ only.

δ^2 Order balance for (A.3) gives:

$$\nabla_H \cdot (\sigma_0 \nabla_H \phi_0) + \frac{\partial}{\partial z}\left(\frac{\partial \phi_2}{\partial z}\right) = 0 \tag{3.A.9}$$

Integrating and applying the insulating boundary condition on top and bottom surface gives us the equation

$$\nabla_H \cdot (\sigma_0 \nabla_H \phi_0) = 0 \tag{3.A.10}$$

Therefore, from above equation we get

$$\left(\frac{\partial \phi_2}{\partial z}\right) = 0 \tag{3.A.11}$$

δ^3 Order balance for (A.3) gives:

$$\nabla_H \cdot (\sigma_1 \nabla_H \phi_0) + \nabla_H \cdot (\sigma_0 \nabla_H \phi_1) + \frac{\partial}{\partial z}\left(\frac{\partial \phi_3}{\partial z}\right) = 0 \quad (3.A.12)$$

Integrating and applying the insulating boundary condition on top and bottom surface gives us the equation

$$\nabla_{\mathrm{H}} \cdot (\sigma_1 \nabla_H \phi_0) + \nabla_H \cdot (\sigma_0 \nabla_H \phi_1) = 0 \quad (3.A.13)$$

To obtain the final depth average equation we perform (3.A.10) + δ× (3.A.13)

$$\nabla_H \cdot (\sigma \nabla_H \bar{\phi}) = 0 \quad (3.A.14)$$

This final equation for the DC Electric field retains its original form of the 3D equation. It can be written as:

$$\nabla_H \cdot (\sigma E_{DC}) = 0 \quad (3.A.15)$$

Where $E_{DC} = -\nabla \phi_{DC}$ and ϕ_{DC} is the applied DC Electric potential at the electrode.

3.2 Flow Field.

Similar to electric field equation we need to find the depth average equation for the flow field. An asymptotic analysis is done similar to what we did in electric field equation. For an incompressible fluid, the flow field is governed by continuity equation and modified Stokes equation [98] because the Reynolds no is much smaller than one [98, 103]. Both these equations are shown below.

$$0 = -\nabla p + \nabla \cdot (\eta \nabla u) + \langle \rho_e E - 0.5 E^2 \nabla \varepsilon \rangle \quad (3.B.1)$$

$$\nabla \cdot u = 0 \quad (3.B.2)$$

$$\langle f_e \rangle = \langle \rho_e E - 0.5 E^2 \nabla \varepsilon \rangle \quad (3.B.3)$$

Where $\langle f_e \rangle$ is the electrothermal body force. It is the summation of Coulomb force $(\rho_e E)$ and dielectric force $(0.5E^2\nabla\varepsilon)$ [98], ρ_e is the free charge density given by Poisson's equation, $\rho_e = \nabla \cdot (\varepsilon E)$ p is the pressure and η is the dynamic viscosity of the fluid.

The slip velocity is on the upper and lower side of the wall (x and y), and is given by the following equations:

$$u = -\varepsilon\zeta_w E/\eta \quad \text{And} \quad w = 0 \tag{3.B.4}$$

$$Re_d = \frac{\rho U_{ev} d}{\mu}$$

The Non-dimensionalized form of the equation can be written as:

For continuity equation,

$$\nabla_H \cdot u + \frac{\partial w}{\partial z} = 0 \tag{3.B.5}$$

Along X and Y directions,

$$Re_d \delta \left(\frac{\partial u}{\partial t} + u \cdot \nabla u\right) = -\nabla_H p + \delta^2 \nabla_H^2 u + \frac{\partial^2 u}{\partial z^2} + \left(\nabla_H^2 \phi + \frac{1}{\delta^2}\frac{\partial^2 \phi}{\partial z^2}\right)\nabla_H \phi \tag{3.B.6}$$

Along Z direction,

$$Re_d \delta^3 \left(\frac{\partial w}{\partial t} + u \cdot \nabla w\right) = -\frac{\partial p}{\partial z} + \delta^4 \nabla_H^2 w + \delta^2 \frac{\partial^2 w}{\partial z^2} + \left(\nabla_H^2 \phi + \frac{1}{\delta^2}\frac{\partial^2 \phi}{\partial z^2}\right)\frac{\partial \phi}{\partial z} \tag{3.B.7}$$

Performing an δ^0 order balance for (3.B.5) – (3.B.7):

$$\nabla_H \cdot u_0 + \frac{\partial w_0}{\partial z} = 0 \tag{3.B.8}$$

$$0 = -\nabla_H p_0 + \frac{\partial^2 u_0}{\partial z^2} + \nabla_H^2 \phi_0 \nabla_H \phi_0 \tag{3.B.9}$$

$$0 = -\frac{\partial p_0}{\partial z} \tag{3.B.10}$$

From equation (3.B.10), we can see that p_0 is not a function of z. Therefore, we can write $p_0 = p_0(x, y)$.

After doing the order analysis of equation (3.B.6) and (3.B.7) we can say that gradients of ϕ_0,ϕ_1, ϕ_2, η and ε with respect to z will be zero.

Also, the third term is independent of z-direction, so taking A= $\nabla_H^2 \phi_0 \nabla_H \phi_0$

Integrating equation (3.B.9), we get

$$u_0 = (\nabla_H p_0 - A)\left(\frac{z^2}{2}\right) + C_1 z + C_2 \tag{3.B.11}$$

C_1 and C_2 are constant of integration. Applying the boundary condition at $u_0 = u_{eo0}$ at $z = \pm 1$, we get

$$u_0 = (\nabla_H p_0 - A)\left(\frac{z^2-1}{2}\right) + u_{eo0} \tag{3.B.12}$$

Depth averaging equation (3.B.12) gives:

$$\overline{u_0} = \frac{-1}{3}(\nabla_H p_0 - A) + u_{eo0} \tag{3.B.13}$$

Also, considering the first term on right-hand side of equation (3.B.13) as

$$\overline{U_0} = \frac{-1}{3}(\nabla_H p_0 - A) \tag{3.B.14}$$

We get on substituting equation (3.B.14) in equation (3.B.13)

$$u_0 = \overline{u_0} + \overline{U_0}\left(\frac{1}{2} - \frac{3z^2}{2}\right) \tag{3.B.15}$$

Depth averaging eq. (3.B.8) we get

$$\nabla_H \cdot \overline{u_0} + \frac{1}{2}\int_{-1}^{1} \frac{\partial w_0}{\partial z} = 0$$

Applying the boundary condition, $w_0 = 0$ at z $= \pm 1$,

$$\nabla_H \cdot \overline{u_0} = 0 \tag{3.B.16}$$

To calculate w_0 we will be integrating equation (3.B.8) and substituting equation (3.B.15), we get

$$w_0 = \nabla_H \cdot \overline{U_0}\left(\frac{z^3}{2} - \frac{z}{2}\right) \tag{3.B.17}$$

Performing an δ^1order balance for (3.B.2), we obtain,

$$Re_d\left(\frac{\partial u_0}{\partial t} + u_0 \cdot \nabla_H u_0 + w_0 \frac{\partial u_0}{\partial z}\right) = -\nabla_H p_1 + \frac{\partial^2 u_1}{\partial z^2} + \nabla_H^2 \phi_0 \nabla_H \phi_1 + \nabla_H^2 \phi_1 \nabla_H \phi_0 + \frac{\partial^2 \phi_3}{\partial z^2}\nabla_H \phi_0 \tag{3.B.18}$$

$$0 = -\frac{\partial p_1}{\partial z} \tag{3.B.19}$$

The 2nd and 3rd term on Right-hand side is independent of z-direction, so

Let $\nabla_H^2 \phi_0 \nabla_H \phi_1 + \nabla_H^2 \phi_1 \nabla_H \phi_0 =$ A

Integrating equation, we get,

$$u_1 = Re_d\left(\frac{\partial u_0}{\partial t} + u_0 \cdot \nabla_H u_0 + w_0 \frac{\partial u_0}{\partial z}\right)\frac{z^2}{2} + \left(\frac{\nabla_H p_1 - A}{\eta}\right)\frac{z^2}{2} + c_1 z + c_2 \tag{3.B.20}$$

Here c_1 and c_2 are constants of integration. Applying the boundary conditions $u_1 = u_{eo1}$ at z $= \pm 1$ to Eq. (3.B.20) and depth averaging, while neglecting high order terms gives

$$\overline{u_1} = Re_d\left[\frac{-1}{3}\left(\frac{\partial \overline{u_0}}{\partial t} + \overline{u_0} \cdot \nabla_H \overline{u_0}\right)\right] - \frac{1}{3}(\nabla_H p_1 - A) + u_{eo1} \tag{3.B.21}$$

On rearranging

$$Re_d\left(\frac{\partial\overline{u_0}}{\partial t}+\overline{u_0}\cdot\nabla_H\overline{u_0}\right)=-\nabla_H p_1+A-3(\overline{u_1}-u_{eo1}) \qquad \text{or}$$

$$Re_d\left(\frac{\partial\overline{u_0}}{\partial t}+\overline{u_0}\cdot\nabla_H\overline{u_0}\right)=\ -\nabla_H p_1+\nabla_H^2\phi_0\nabla_H\phi_1+\nabla_H^2\phi_1\nabla_H\phi_0-3(\overline{u_1}-u_{eo1}) \tag{3.B.22}$$

Performing an δ^2order balance for (3.B.2), we obtain,

$$Re_d\left(\frac{\partial\overline{u_1}}{\partial t}+\overline{u_1}\cdot\nabla_H\overline{u_0}+\overline{u_0}\cdot\nabla_H\overline{u_1}\right)=-\nabla_H p_2+\frac{\partial}{\partial z}\left(\frac{\partial \boldsymbol{u_2}}{\partial z}\right)+\nabla_H^2\phi_0\nabla_H\phi_2+ \nabla_H^2\phi_2\nabla_H\phi_0+\nabla_H^2\phi_1\nabla_H\phi_1 \tag{3.B.23}$$

$$0=-\frac{\partial p_2}{\partial z}+\frac{\partial^2 w_0}{\partial z^2} \tag{3.B.24}$$

$$\nabla_H\cdot u_2+\frac{\partial w_2}{\partial z}=0 \tag{3.B.25}$$

The last three terms on the right-hand side are independent of z and are written as:

$$E=\nabla_H^2\phi_0\nabla_H\phi_2+\nabla_H^2\phi_2\nabla_H\phi_0+\nabla_H^2\phi_1\nabla_H\phi_1$$

Therefore, the equation can be written as

$$Re_d\left(\frac{\partial\overline{u_1}}{\partial t}+\overline{u_1}\cdot\nabla_H\overline{u_0}+\overline{u_0}\cdot\nabla_H\overline{u_1}\right)=-\nabla_H p_2+\frac{\partial}{\partial z}\left(\frac{\partial u_2}{\partial z}\right)+E \tag{3.B.26}$$

Integrating the above equation, applying Boundary condition $u_2=u_{eo2}$ at $z=\pm1$ and depth averaging we get:

$$Re_d\left(\frac{\partial\overline{u_1}}{\partial t}+\overline{u_1}\cdot\nabla_H\overline{u_0}+\overline{u_0}\cdot\nabla_H\overline{u_1}\right)=-\nabla_H p_2+E+\nabla_H^2\overline{u_0}-3(\overline{u_2}-u_{eo2}) \tag{3.B.27}$$

To obtain the final depth average equation, we need to do asymptotic analysis by adding (B.14) + δ × (B.18) + δ^2 × (B.22) we obtain,

$$Re_d\delta\left(\frac{\partial\bar{u}}{\partial t}+\bar{u}.\nabla_H\bar{u}\right)=-\nabla_H p+\delta^2\nabla_H^2\bar{u}-3(\bar{u}-u_{eo})+\nabla_H^2\phi\nabla_H\phi$$

3.3 Mass Transport Equation

The convective diffusion equation is applied across the fluid domain of the model. The particle size used is small, so the working fluid can be assumed as a continuum of the dilute solution. The following equation represents the mathematical form of the equation.

$$\frac{\partial \mathrm{c}}{\partial \mathrm{t}} + \mathrm{v} \cdot \nabla \mathrm{c} = \mathrm{D}\nabla^2 \mathrm{c}$$

Where c is the molar concentration of particle, v is the velocity and D is the diffusion coefficient. A depth average analysis is being done in a similar fashion as the previous equations. The details of the depth average equation are presented below:

Expanding the above equation

$$\frac{\partial c}{\partial t} + \left(u + u_{ep}\right)\frac{\partial c}{\partial x} + \left(v + v_{ep}\right)\frac{\partial c}{\partial y} + \left(w + w_{ep}\right)\frac{\partial c}{\partial z} + c\left(\nabla . u_{ep}\right) = D\left(\frac{\partial^2 c}{\partial x^2} + \frac{\partial^2 c}{\partial y^2} + \frac{\partial^2 c}{\partial z^2}\right) \quad (3.C.1)$$

Expanding the LHS of above equation, we get

$$\frac{\partial c}{\partial t} + u\frac{\partial c}{\partial x} + v\frac{\partial c}{\partial y} + w\frac{\partial c}{\partial z} + u_{ep}\frac{\partial c}{\partial x} + v_{ep}\frac{\partial c}{\partial y} + w_{ep}\frac{\partial c}{\partial z} + c\left(\frac{\partial u_{ep}}{\partial x} + \frac{\partial v_{ep}}{\partial y} + \frac{\partial w_{ep}}{\partial z}\right) = R.H.S$$

Let $u_{ep}\frac{\partial c}{\partial x} + v_{ep}\frac{\partial c}{\partial y} + w_{ep}\frac{\partial c}{\partial z} = A$

$$c\left(\frac{\partial u_{ep}}{\partial x} + \frac{\partial v_{ep}}{\partial y} + \frac{\partial w_{ep}}{\partial z}\right) = B$$

Substituting values of u_{ep}, v_{ep}, w_{ep} *in A*, we get

$U_{ep} = p_a E$, $p_e = \frac{U_{ev} d}{D}$ and $p'_a = p_a c' \varphi_o$

$A = \frac{C_o P_a \varphi_0}{H^2} (\nabla_H \varphi . \nabla_H c + \frac{1}{\delta^2} \frac{\partial \phi}{\partial z} \frac{\partial c}{\partial z})$

$B = \frac{C_o P_a \varphi_0}{H^2} (\nabla_H^2 \varphi + \frac{1}{\delta^2} \frac{\partial^2 \phi}{\partial z^2})$

Substituting back in equation (3.C.1), we get

$$P_e \delta \left(\frac{\partial c}{\partial t} + v \cdot \nabla c\right) - \frac{P'_a \delta^2}{D} (\nabla_H \varphi . \nabla_H c + c \nabla_H^2 \varphi + \frac{1}{\delta^2} \left(\frac{\partial \phi}{\partial z} \frac{\partial c}{\partial z} + c \frac{\partial^2 \phi}{\partial z^2}\right)) = (\delta^2 \nabla_H^2 c + \frac{\partial^2 c}{\partial z^2}) \quad \text{(3.C.2)}$$

At the δ^0-order, we have

$$\frac{\partial^2 c_0}{\partial z^2} = 0 \quad \text{(3.C.3)}$$

Applying the boundary condition $\frac{\partial c_0}{\partial z} = 0$ at z $= \pm 1$ we get:

$$c = c_0(x, y, t) \quad \text{(3.C.4)}$$

At the δ^1-order, we have

$$P_e \left(\frac{\partial c_0}{\partial t} + \mathrm{u}_0 \cdot \nabla_H c_0\right) = \frac{\partial^2 c_1}{\partial z^2} \quad \text{(3.C.5)}$$

Depth-averaging and applying the boundary condition, we get

$$\int_{-1}^{1} \frac{\partial^2 c_1}{\partial z^2} dz = \int_{-1}^{1} P_e \left(\frac{\partial c_0}{\partial t} + \mathrm{u}_0 \cdot \nabla_H c_0\right) dz \quad \text{(3.C.6)}$$

Therefore, we have

$$\frac{\partial c_0}{\partial t} + \overline{\mathrm{u}_0} \cdot \nabla_H c_0 = 0 \quad \text{(3.C.7)}$$

On integrating equation (3.C.6) in the z direction we get,

$$\frac{\partial c_1}{\partial z} = P_e\left[\frac{\partial c_0}{\partial t}z + (\overline{\mathrm{u}_0}\cdot\nabla_H c_0)z + (\overline{\mathrm{U}_0}\cdot\nabla_H c_0)\left(\frac{1}{2}z - \frac{1}{2}z^3\right)\right] + A_0 \quad (3.C.8)$$

Applying the Boundary conditions integrating equation (3.C.8), we get

$$c_1 = P_e(\overline{\mathrm{U}_0}\cdot\nabla_H c_0)\left(\frac{1}{4}z^2 - \frac{1}{8}z^4\right) + A_1 \quad (3.C.9)$$

Depth averaging the above equation gives us

$$c_1 = \bar{c_1} + \frac{1}{4}P_e(\overline{\mathrm{U}_0}\cdot\nabla_H c_0)\left(-\frac{7}{30} + z^2 - \frac{1}{2}z^4\right) \quad (3.C.10)$$

For the δ^2 we have the following equation

$$P_e\left(\frac{\partial c_1}{\partial t} + \mathrm{u}_1\cdot\nabla_H c_0 + \mathrm{u}_0\cdot\nabla_H c_1 + w_0\frac{\partial c_1}{\partial z} + w_0\frac{\partial c_1}{\partial z}\right) - \frac{P'_a}{D}(\nabla_H\varphi.\nabla_H c + c\nabla_H^2\varphi)$$
$$= \nabla_H^2 c_0 + \frac{\partial^2 c_2}{\partial z^2} \quad (3.C.11)$$

Depth averaging the above equation and applying the boundary condition gives:

$$P_e\left(\frac{\partial\overline{c_1}}{\partial t} + \overline{\mathrm{u}_1}\cdot\nabla_H c_0 + \overline{\mathrm{u}_0\cdot\nabla_H c_1} + \overline{w_0\frac{\partial c_1}{\partial z}}\right) - \frac{P'_a}{D}(\nabla_H\varphi.\nabla_H c + c\nabla_H^2\varphi) = \nabla_H^2 c_0 \quad (3.C.12)$$

Substituting for the expressions for u_0, w_0, and c_1, and expanding (3.C.12) we get,

$$\frac{\partial\overline{c_1}}{\partial t} + \overline{\mathrm{u}_1}\cdot\nabla_H c_0 + \overline{\mathrm{u}_0}\cdot\nabla_H\bar{c_1} - \frac{P'_a}{D}(\nabla_H\varphi.\nabla_H c + c\nabla_H^2\varphi) = \frac{1}{P_e}\nabla_H^2 c_0 + \frac{2}{105}P_e\big[(\overline{\mathrm{U}_0}\cdot$$
$$\nabla_H)(\overline{\mathrm{U}_0}\cdot\nabla_H c_0) + (\nabla_H\cdot\overline{\mathrm{U}_0})(\overline{\mathrm{U}_0}\cdot\nabla_H c_0)\big] \quad (3.C.13)$$

Performing (3.C.7) + δ ×(3.C.13), we obtain

$$\frac{\partial\bar{c}}{\partial t} + \nabla_H.(\bar{\mathrm{u}}_p.\bar{c}) = \frac{P'_a}{D}(\nabla_H\bar{\varphi}.\nabla_H\bar{c} + \bar{c}\nabla_H^2\bar{\varphi}) + \frac{\delta}{P_e}\nabla_H^2\bar{c} + \frac{2}{105}P_e\delta[\nabla_H.(\overline{U}\cdot(\overline{U}\cdot$$
$$\nabla_H\bar{c}))] \quad (3.C.14)$$

Where $u_p = u + u_{ep}$

3.4. Energy Equation

When an electric field is applied across the microchannel, the joule-heating effect is observed to take place as explained in the earlier chapter. Due to Joule heating, a rise in temperature takes place across the microchannel and PDMS. This heat generated is dissipated in all directions across the model. Heat transfer through convection takes places from the top and sidewalls of PDMS and top surface of the reservoir, by conduction from the bottom side of PDMS and between glass, film, and PDMS. The energy equation is given by [98]

$$\rho C_p \left(\frac{\partial T}{\partial t} + \mathrm{u} \cdot \nabla T\right) = \nabla \cdot (k \nabla T) + \sigma \langle \mathrm{E}^2 \rangle \tag{3.D.1}$$

The boundary conditions are:

$\frac{\partial T}{\partial z} = -\frac{1}{k}\frac{(T-T_\infty)}{R_{us}}$ at the top surface.

$\frac{\partial T}{\partial z} = \frac{1}{k}\frac{(T-T_\infty)}{R_{ls}}$ at the bottom surface.

Non-Dimensionalizing the above equation by substituting with $Z' = \frac{\sigma E_0^2 d^2}{k T_\infty}$ and $p' = \frac{\rho C_p U_{ev} d}{k}$

$$p'\delta \left(\frac{\partial T}{\partial t} + u \cdot \nabla T\right) = \delta^2 \nabla_H^2 T + \frac{\partial^2 T}{\partial z^2} + Z' \left(\nabla_H \phi \nabla_H \phi + \frac{1}{\delta^2}\left(\frac{\partial \phi}{\partial z}\right)^2\right) \tag{3.D.2}$$

Performing δ^0 order balance on (3.D.2):

$$0 = \frac{\partial^2 T_0}{\partial z^2} + Z' e \nabla_H \phi_0 \nabla_H \phi_0 \tag{3.D.3}$$

Depth averaging and applying the following boundary conditions yields:

$$0 = \frac{q_{u0} - q_{l0}}{2} + Z'(\nabla_H \phi_0 \nabla_H \phi_0) \tag{3.D.4}$$

Performing a δ^1 order balance for Eq. (3.D.2):

$$P'\left(\frac{\partial T_0}{\partial t} + u_0 \cdot \nabla_H T_0 + w_0 \frac{\partial T_0}{\partial z}\right) = \frac{\partial^2 T_1}{\partial z^2} + 2\, Z'(\nabla_H \phi_1 \nabla_H \phi_0) \tag{3.D.5}$$

Depth averaging and applying the following boundary conditions yields:

$$P'\left(\frac{\partial \overline{T_0}}{\partial t} + \overline{u_0 \cdot \nabla_H T_0} + \overline{w_0 \frac{\partial T_0}{\partial z}}\right) = \frac{\partial^2 \overline{T_1}}{\partial z^2} + 2\,\overline{Z'(\nabla_H \phi_1 \nabla_H \phi_0)} \tag{3.D.6}$$

To obtain the final depth average equation, we need to do asymptotic analysis by adding (3.D.4) + δ × (3.D.6)

The simplification leads to:

$$P'\delta\left[\frac{\partial \bar{T}}{\partial t} + \bar{u}\ \cdot \nabla_H \bar{T}\right] = \delta^2 {\nabla_H}^2 \bar{T} + \frac{q_u - q_l}{2} +\ Z'(\nabla_H \phi \nabla_H \phi) \tag{3.D.7}$$

On arriving at the Eq. (3.D.7), we have arbitrarily added or dropped terms without losing the asymptotic consistency [97,102].

3.5 Boundary Conditions

The above-explained equations of electric current, flow field, concentration equation, and energy equation are coupled together and solved simultaneously in the numerical model. The electric current, flow field, concentration equation are solved for the microchannel region only while energy equation is solved for both microchannel and PDMS region. Different boundary conditions are associated with the above-mentioned equations and are explained below.

3.5.1 Electric current

The electric field is confined to the microchannel region so an insulating boundary condition ($\mathrm{n} \cdot \left(\sigma \nabla \phi_{DC}\right) = 0$, n is the unit normal vector) is imposed on all the sidewalls of the microchannel. Electric potential is applied at the two opposite ends of the channel, which is shown by two holes. Since the electrodes are made of platinum, they have high electrical and thermal conductivities; they are hence treated as holes in 2D modeling. At the inlet channel electrode, we apply ϕ_{DC} voltage and ground potential on the outlet channel electrode.

3.5.2 Fluid flow field

Since there is no pressure driven flow in our model, we apply a boundary condition of P=0 at two ends of the microchannel. A no slip u=0 boundary condition is applied on the electrode surface because the local electric field is normal to the surface. Smoluchowski electroosmotic slip velocity condition is applied on the on the top wall of the channel and reservoir. EDL is very small as compared to the width of the channel and hence we apply can apply the slip velocity boundary condition. Since our model is symmetric about horizontal axis, a symmetry boundary condition is also applied on the bottom wall of the channel.

3.5.3 Mass transport

This is also confined to the microchannel region of the geometry. An initial uniform concentration of C=1 mol/m^3 is applied to the fluid domain. All the channel boundaries except for the symmetry plane are insulated for mass transport equation.

3.5.4 Temperature Field

Both the microchannel(fluid) and PDMS(solid) regions are selected for temperature field since heat diffusion takes places via conduction from channel to PDMS and then to surrounding via convection. Since the electrodes have high thermal conductivity, there is no temperature drop inside them and an isothermal boundary condition (T=T_∞) is applied on them.

CHAPTER FOUR

RESULTS AND DISCUSSION

4.1 Introduction

In this chapter, we will discuss both the numerical and experimental results that we obtained from our work done. DEP forces depend on the size of the particle. The DEP force is directly proportional to the cube of the size of the particle. Since the size of the particle is small, the difficulty of trapping and pre-concentration increases greatly [38]. To compensate for the weak DEP force due to small size of particle we need to greatly enhance the electric field. This increase in electric field would help to improve trapping of the particle. Due to the above-mentioned reason, the insulator based DEP or iDEP devices seems to be as reasonably choice to trap sub micro species. In iDEP devices, non-uniform cross section of the microchannel geometry is used to develop temperature gradients. In addition, the use of a high conductivity buffer solution ensures a better throughput of the system [104]. However, with these advantages there is a major phenomenon that comes into play when a high electric field is used in combination with high conductivity buffer solution, which is called as Joule heating. Therefore, the iDEP devices serve as a much better choice for the trapping of sub-micrometer sized particles.

Due to the joule heating effect, there is an electrothermal flow induced, which exerts a drag force. This drag force then competes with the drag force applied by the nDEP. The two forces then together affect the electrokinetic motion of the suspended species. Since the size of the sub-micron particle is small, the electrothermal drag force dominates flow

over the drag force due to nDEP. In fact, the electrothermal drag force is expected to effectively dominate the motion at the insulating constriction. This work deals with the development of a model, which could be used to manipulate the motion of sub-micron species by using electrothermal flow. A region of multiple constrictions is generated called as ratchet microchannel. The experimentally obtained results are compared with the numerically obtained results.

4.2 Experimental and numerical results and discussions

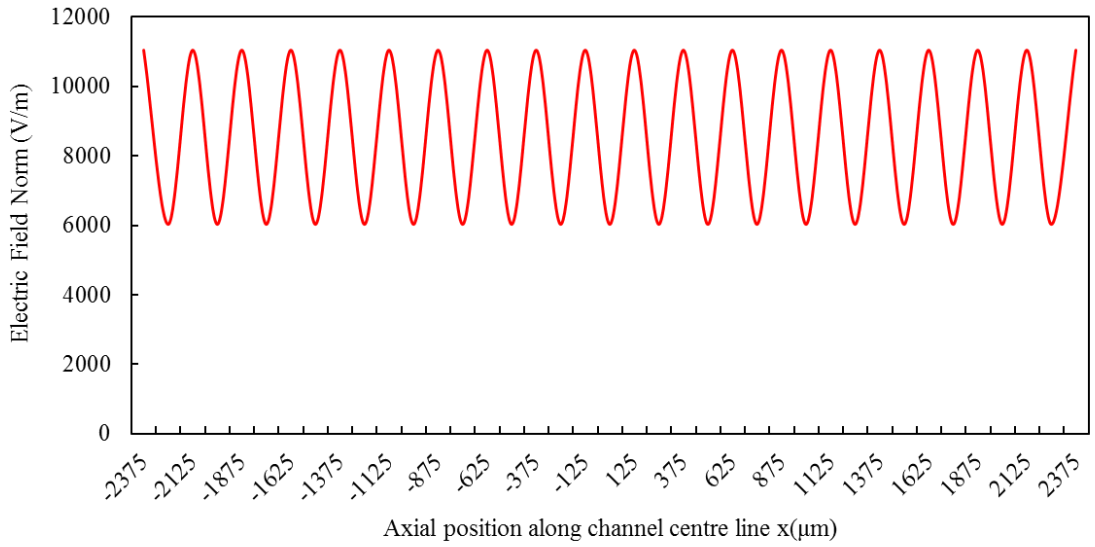

Figure 4.1. Variation of electric field at the channel centerline along the length of the ratchet microchannel channel for 50V DC applied electric field.

Figure 4.1 represents the variation of electric field at the channel centerline along the length of microchannel. The applied voltage is 50V DC. As per current conservation law,

the local amplification in electric field can be seen due to potential drop. Since our model has a ratchet geometry with multiple constrictions, periodic oscillations of electric field can be seen at each ratchet. These sharp peaks due to ratchet geometry gives us multiple regions of interest for manipulating motion of species.

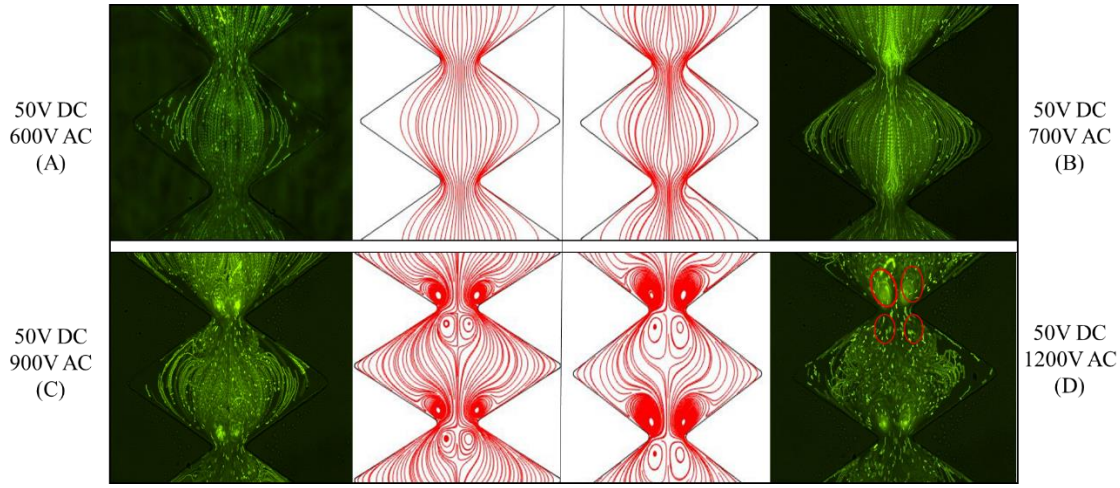

Figure 4.2. Experimentally obtained superimposed path lines are compared with the numerically predicted streamlines for different AC/DC ratio. The development of electrothermal vortices can be seen for 0.5-micron particles with the increasing AC/DC ratio. The direction of the electroosmotic fluid flow is from top to bottom while the direction of the tracing particle is from bottom to top due to the dominance of the electrophoresis over electroosmotic flow. The arrowed loop in the 50V DC and 1200V AC shows the direction of the electrothermal vortices.

Figure 4.2 shows a comparison between the experimentally obtained streamlines and numerically obtained streamlines for a 50V DC biased AC Voltage at the tip of the ratchets. To obtain the experimental streak images, we superimpose images at every instant over the whole length of the video. It can be conclude that up to 600V AC voltage, the particle

mostly follow the path of the electric field lines. The electrokinetic motion is dominant at this voltage and the electrothermal flow is not strong enough to overcome its effect. At 700V AC voltage we can see that the electrothermal flow start to show its effect or the joule heating effect can be noticed. The particle then can be seen to follow streamlines of electrothermal flow. As we increase the AC/DC ratio the joule heating effect increase and the size of the vortices around the ratchet increases. We change the AC/DC ratio from 12(600 AC/50V DC) Fig 4.2A, 14(700V AC/50V DC) Fig 4.2B, 18(900V AC/50V DC) Fig 4.2C to 24(1200V AC/50V DC) Fig 4.2D and consequently we can see the significant increase in the size of the two vortices.

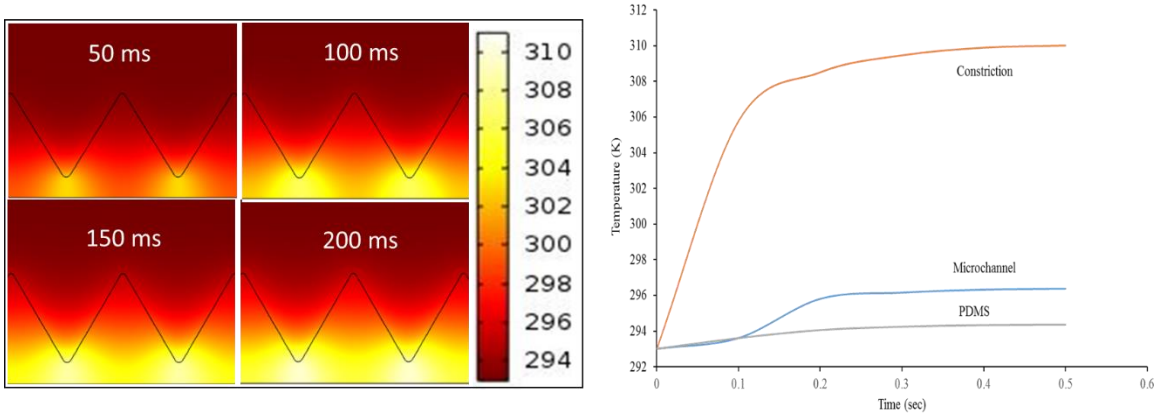

Figure 4.3. The part A shows the numerically predicted development of temperature field contour around the ratchet channel region of the computational domain. The part B of the figure shows the development of temperature at three different locations with the passage of time.

Figure 4.3a shows the development of temperature field with the passage of time. The temperature field is completely developed after about 200 ms. The electric field as explained previously develops almost instantaneously after is it applied, so the joule heating effect and the temperature rise in the constriction region also happen very rapidly

within milliseconds. After the temperature field is fully developed, the maximum temperature is around 311K. The heat generated in the microchannel region propagates to the other parts of the device and the temperature field develop in a similar fashion with a lower maximum temperature. As predicted in the previous model [105] the temperature profile shifts towards the downstream region of the microchannel due to fluid flow.

Figure 4.3b shows the temperature-time graph for the constriction, microchannel and PDMS region of the model. The graph for all the three regions follow a similar trend with different peak temperature. Initially, the temperature rises at a faster rate and then increases gradually. The joule heating effect is restricted to the fluid domain, so the initial rate of temperature rise is much greater that the glass and PDMS region. This can be clearly observed from the graph.

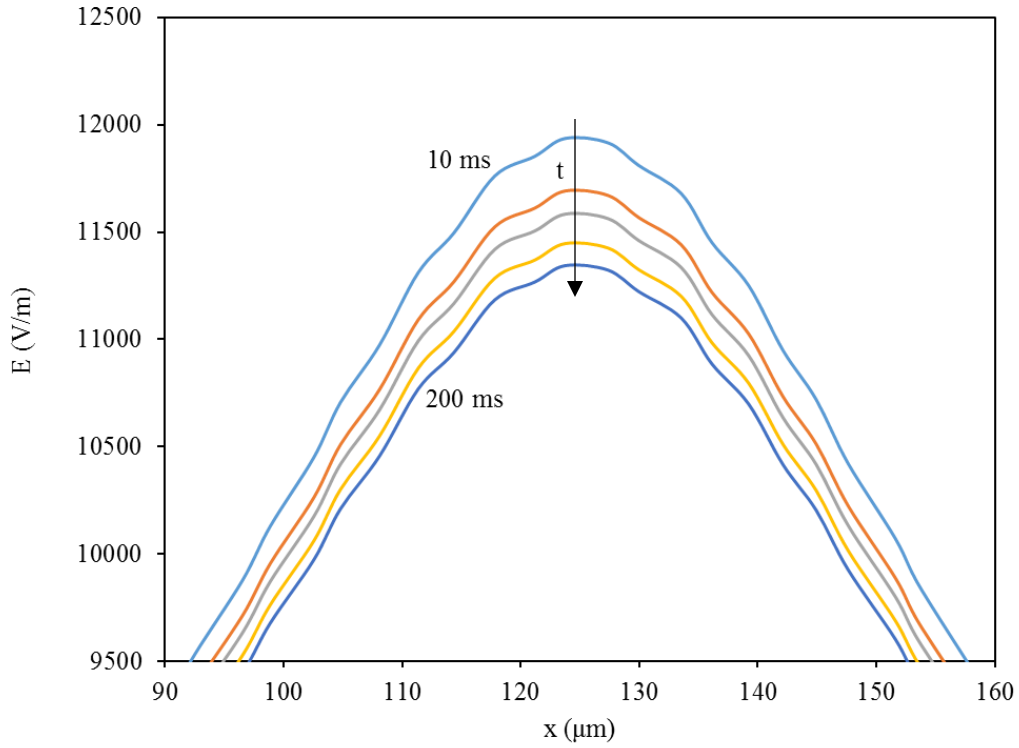

Figure 4.4. Transient development of electric field along the length of the channel centerline in the range of 70μm around the tip of ratchet. The arrow indicates the direction of increase in time starting from 10ms, 20 ms to 200ms.

Figure 4.4 shows the electric field profile around the tip region of the ratchet for different time instant ranging from 0 ms to 200 ms. It can be seen from the graph that electric field profile develops almost instantly at t=0 sec. The electric field profile remains unchanged after 200 ms and is therefore not shown in the figure.

$$\nabla^* \left[C_r(\sigma^* E^*) + \frac{\partial(\in^* E^*)}{\partial t^*} \right] = 0$$

Where $\nabla^* = L_{ref}\nabla, \sigma^* = \frac{\sigma}{\sigma_{ref}}, \in^* = \frac{\in}{\in_{ref}}, E^* = \frac{E}{E_{ref}}, C_r = \frac{t_{ref}}{\frac{\in_{ref}}{\sigma_{ref}}}$

This instantaneous development of electric field can be explained with equation above-mentioned equation of electric field. For further detail into mathematical analysis, users can refer to [97]. The development of electric field is coupled with the temperature field of the fluid domain. The properties are temperature dependent and the temperature field has a transient change. By plugging in the reference values for permittivity and conductivity, the charge relaxation time comes out to be of few nanoseconds. This means that the charge relaxation no reaches very high value almost instantaneously and hence we see that electric field distribution attains steady state almost instantaneously. As the temperature increases, the electrical conductivity increases and the electric field decreases slightly as per the current conservation law. As shown previously the rate of temperature increase drops with the passage of time and therefore the rate of drop of electric field follows similar trend. The temperature profile almost fully develops at around 200 ms and therefore the electric field almost attains steady state after that.

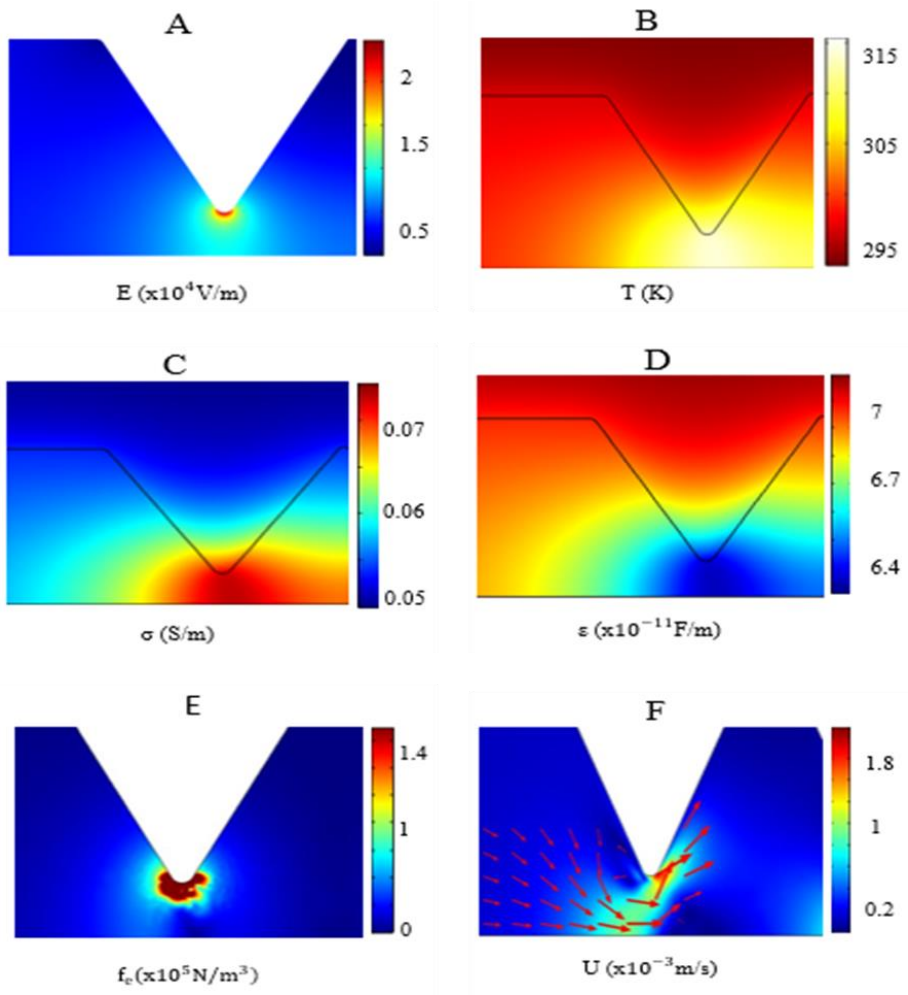

Figure 4.5. Numerically predicted contours of (A). Electric field (B). Temperature field (C). Electrical Conductivity (D). Electric permittivity €. Electrothermal body force (F). Velocity Field at the constriction region of a ratchet for 50V DC and 900V AC Voltage.

Figure 4.5 illustrates the development of electrothermal fluid circulations in the electroosmotic entry flow for the case of 50V DC biased 900V AC Voltage. The fluid properties as explained previously are temperature dependent. The constriction region has smaller area as compared to the reservoir region. Due to this the electric field amplifies in the constriction region. This can be illustrated in figure 4.5A. Due to this amplified electric

field, the joule heating takes places in the constriction region, which in turn raises the fluid temperature. This can be illustrated in figure 4.5B Due to these temperature gradients, non-uniformities occur in the fluid properties. The electric conductivity increases by almost 50 percent, illustrated in figure 4.5C and the electrical permittivity decreases by almost 10 percent, illustrated in figure 4.5D. When DC biased AC field acts on these gradients in fluid properties, it induces electrothermal body force and is illustrated in figure 4.5E. The elecrothermal body force i.e. $f_e$can be expressed by equation (3.B.3.), its magnitude is higher near the walls of channel than the centerline of channel, and hence the local fluid velocity is reversed. This gives rise to electrothermal fluid circulations. Electrothermal fluid circulations can be illustrated in figure 4.5F.

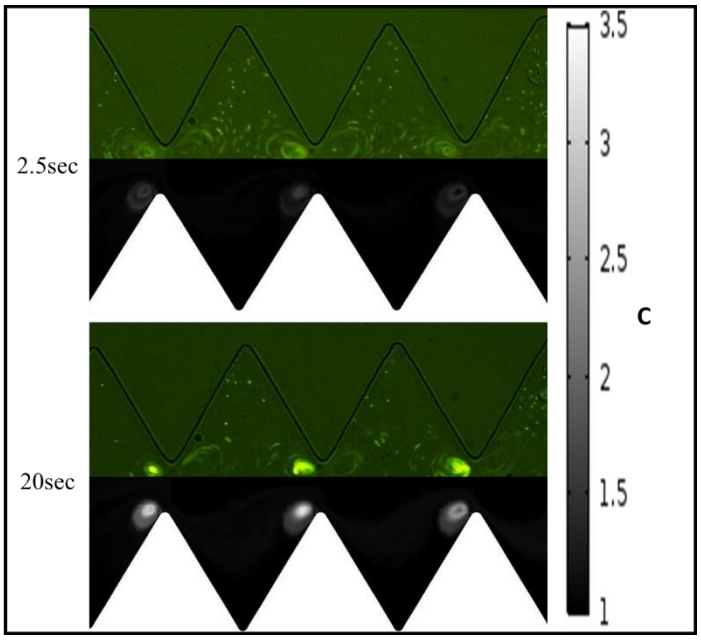

Figure 4.6. Comparison of experimental obtained snapshot and numerically predicted increase in particle entrainment within the vortices at the constriction region of ratchet microchannel with the increase in time.

The trapping of sub-micron particle takes place at the region where electrothermal vortices are formed in the channel. The claim can further be justified with the help of concentration distribution of the particles in the microchannel region. Figure 4.6 represents a comparison between the experimentally obtained snapshot of the particle constriction with the numerically predicted concentration distribution of the particle at different times. The applied voltage is 50V DC and 1000V AC. The increase for particle concentration within the vortices with the increase in time can be seen in the experimental snapshot. In the experimental image the particle can be seen to be trapped exclusively in the downstream vortices around the ratchet tip. The reason for this kind of behavior is due to the direction of rotation of electrothermal vortices. The electrothermal drag force interacts with the particles at the upstream vortices and pulls the incoming particle with the flow. The particles are then pushed towards the downstream vortices. The direction of rotation of electrothermal flow in the downstream regions is opposite in direction and therefore it tends to momentarily retard the particle motion, thereby facilitating entrainment of the particles [97]. The numerical simulations results can be seen to predict the similar kind of particle entrainment behavior and increase in the concentration of particle at each vortex.

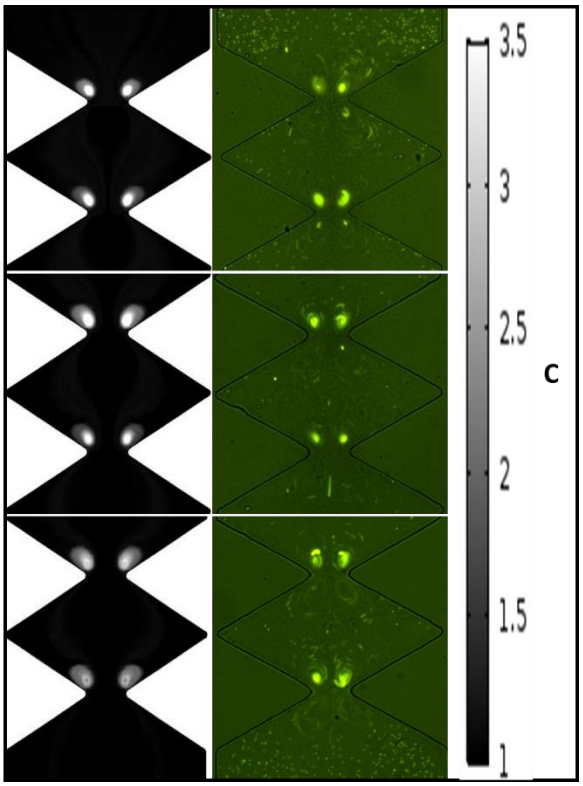

Figure 4.7. Electrothermal trapping zones at 20 seconds across the length of the microchannel for a 0.5-micron particle.

Figure 4.7 shows the comparison between the experimental obtained and numerically predicted concentration increase over the length of the ratchet channel at 20 second. From figure 4.7 the concentration is seen to decrease as we move from the outlet of the channel to the inlet in the direction of particle motion. This is because, as the particle moves from outlet of the channel to the inlet of the channel, the concentration available for entrainment decreases. The difference, however is not very large since it is compensated by the initial concentration of the mass which is present near the ratchet region. This mass gets trapped in the downstream vortices and hence effect the local increase in the particle concentration. The experiment is not run for more than 20 seconds since the amount of heat generated in the constriction region becomes very high. Due to this high heat generation

secondary electrothermal forces are induced from lower temperature reservoir to higher temperature constriction region. This high heat generated which in turn induces electrothermal flow damages the micro device and hence limits its functionality [97].

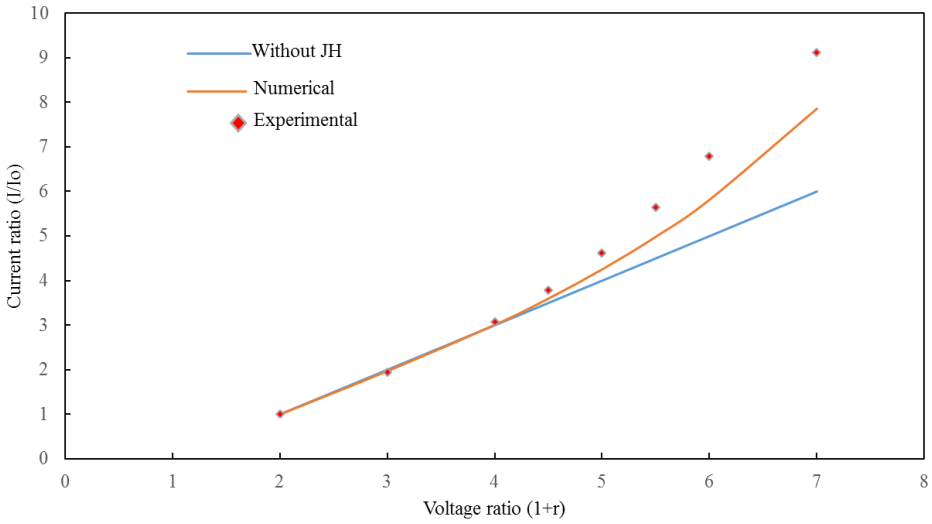

Figure 4.8. Comparison between experimentally measured and numerical predicted rise of current with increase in AC-DC ratio. The non-linear increase of the current is due to joule heating effect caused by change in electrical conductivity due to rise in temperature.

Figure 4.8 shows a comparison between the experimentally and numerically measured current in the microchannel region. The ratio of current is plotted against the AC-DC ratio. For the experimental part, the current is measured at each AC-DC ratio and then the system is left to cool down to ambient temperature before the next set of reading are taken. The numerical results seems to agree reasonably with the experimentally measured values. At higher voltages, due to joule heating the rise in temperature is high, which causes the damage to the PDMS. Due to this damage the thermal properties of the PDMS are altered, thereby making PDMS thermally resistive which results in higher buffer temperature. At low voltage ratio the joule heating is low which does not have a significant

effect on temperature dependent electrical conductivity and hence the graph shows a linear variation. But as the AC-DC ratio increases, the joule heating increases and in turn the high temperature causes a significant change in electric current in the buffer. Due to this increased conductivity, the electric current then follows a non-linear variation as the voltage ratio is further increased. The experimental data used in this thesis is obtained from a single experiment done for symmetric channel for different set of AC voltages.

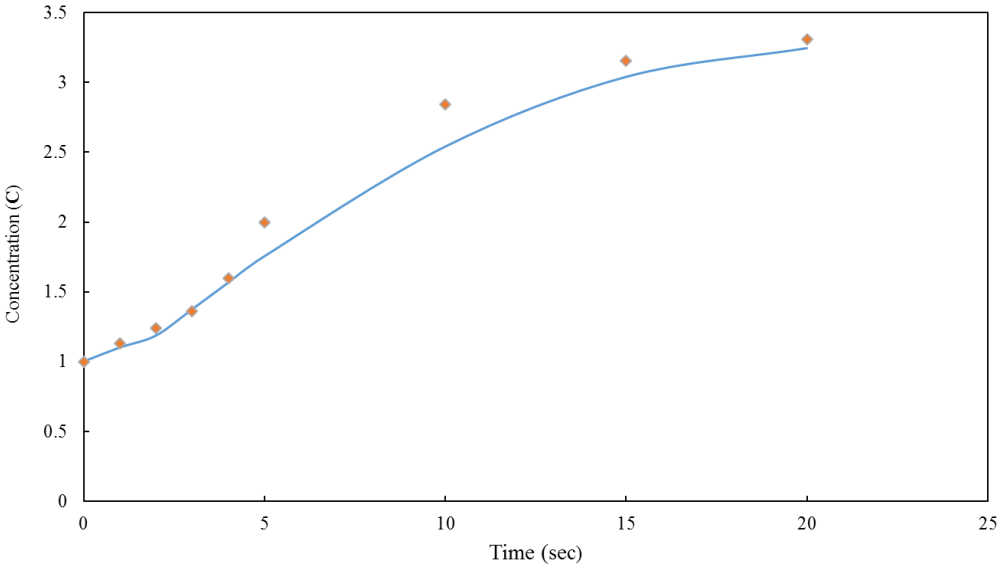

Figure 4.9. This plot shows the comparison between experimental measurements of concentration vs numerically predicted measurement of concentration for a 0.5-micron particle along with increase time.

The above plot shows the comparison between experimentally and numerically predicted rise in concentration with the increase in time. As explained before for small particles electrothermal vortices that generate due to joule heating inside the constriction region can be exploited to trap particles inside them. With this advantage, joule heating has

a disadvantage of heating up the micro device thereby limiting the run time to very small periods of about 20 sec. Therefore we only have data for around 20 seconds because after that the risk of damage to device occurs. From the graph, it can be said that our numerical model is able to predict the results with reasonable accuracy.

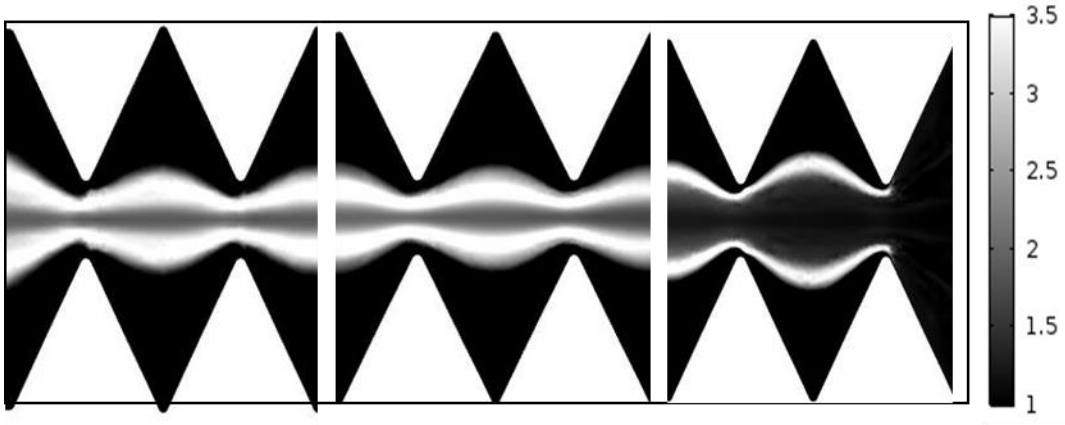

Figure 4.10 the figure shows the numerically predicted concentration distribution for the manipulation of 0.5-micron particle around the center of the ratchet channel when no joule heating is present.

Figure 4.10 shows the concentration plot for the case of only dielectrophoretic manipulation of particles. A 50V DC and 1000V AC voltage is applied across the channel. Joule heating is absent in this case. As we can seen, the particles can be seen converging towards the center of the channel and does not provide a particular trapping zone where particles could be concentrated, however this could be achieved using electrothermal vortices as shown previously. This study further justifies our claim that joule heating enabled particle manipulation is an effective way to trap sub-micron particles.

CHAPTER FIVE

PARAMETRIC STUDY

5.1. Introduction

In this chapter, we examine the effect of different parameters on our experimental and numerical part of the analysis. In the previous chapter the ratchet geometry that we use, is symmetric in nature. We can further examine the results by changing the shape of the ratchet while performing experiments and then develop a numerical model for comparison. For experimental part, the fabrication technique used to manufacture asymmetric ratchet geometries is similar to those used to manufacture symmetric channel (explained in detail in the second chapter) and hence not discussed in detail here. For the numerical modelling, we can simply change the geometry of the model to create asymmetric ratchet channel. All the other material properties and dimension used are same. As we discussed before, a major portion of joule heating is rejected along the depth direction of the channel. The depth of the channel can also be altered to study the effect of joule heating.

5.2 Backward Ratchet channel

The backward channel has the same dimensions as the symmetric channel discussed before. The difference is in the shape of the ratchet. One surface of the ratchet is normally oriented to the channel centerline and the other surface is inclined to the same surface. When we move from the reservoir, which has DC, applied voltage or the inlet reservoir towards the start of the ratchet geometry, if the direction of 1st ratchet surface which comes

in contact with the fluid, is inclined towards the center of the microchannel, then it is termed as backward ratchet channel.

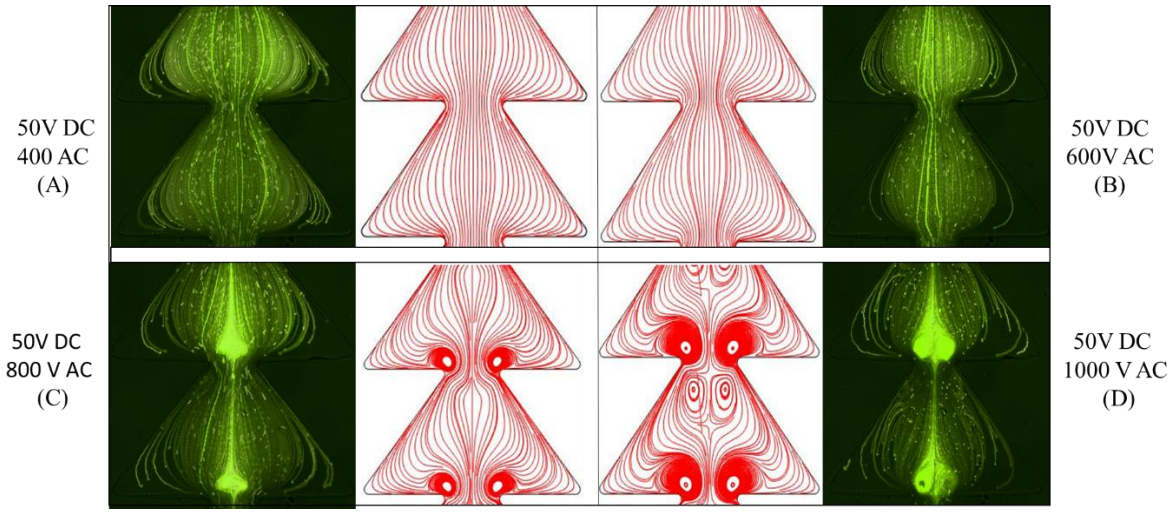

Figure 5.1. shows the comparison between experimentally obtained superimposed images of pathlines for different AC voltages and the numerically predicted image of streamlines for different AC voltages. The development of electrothermal vortices can be seen for 0.5-micron particles with the increasing AC/DC ratio. The arrowed loop in the 50V DC and 1000V AC shows the direction of the electrothermal vortices.

Figure 5.1 shows the comparison between the experimentally obtained superimposed images of pathlines and numerically predicted image of streamlines for a 0.5 micron particle in asymmetric backward ratchet channel geometry. The AC/DC voltage ratio is increased from 50V DC and 400V AC to 50V DC to 1000V AC. The development of the electrothermal vortices is evident from the figures in both experimental and numerical images. For the case of 50V DC/ 400V AC and 50V DC and 600V AC no electrothermal vortices can be seen in both the experimental and numerical images. At these voltages the electrothermal force is not strong enough to overcome the electrokinetic motion. As the AC voltage is further increased to 800V, the joule heating effects starts to come into play

and the electrothermal vortices can be seen to be generated near the constriction region. When the AC voltage is further increased, the size of the electrothermal vortices grows in size and giving rise to two counter rotating vortices.

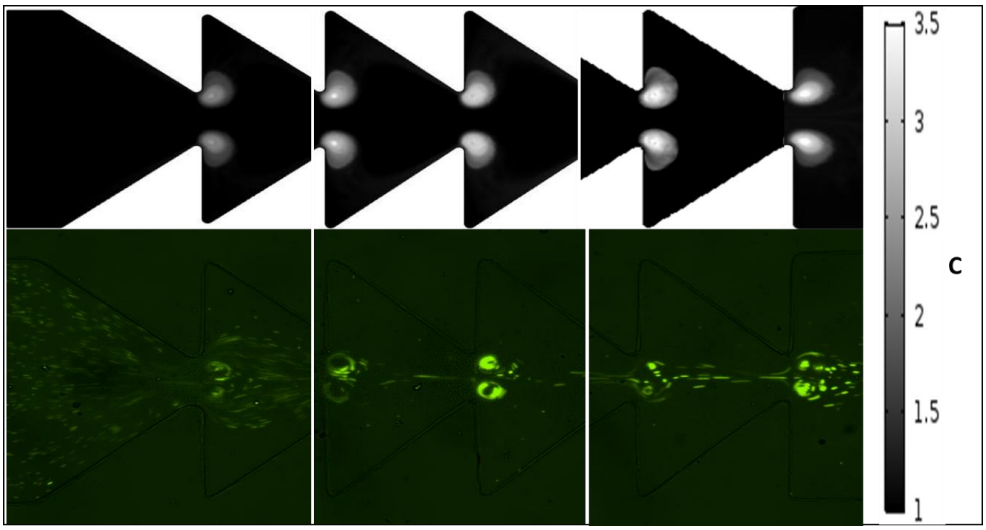

Figure 5.2. Comparison between experimentally obtained images of particle entrainment in the electrothermal vortices and the numerically predicted images of particle entrainment in the vortices for 0.5 micron particle at 20 sec, along the length of the channel.

Figure 5.2 figure shows the comparison between experimentally obtained snapshot and numerically predicted images of particle entrainment within the vortices along the length of the backward ratchet channel. Similar to the way of symmetric ratchet channel, we see a decreasing trend in the concentration of particle as we move from outlet of channel to the inlet of the channel. The numerical results seem to be in agreement with the experimental observations. As for the backward channel we changed the shape of the ratchet, the overall effect in the concentration of particle is not significant.

5.3 Forward ratchet channel

Similar to the way in which we defined the backward channel, the forward channel can be defined. One surface of the ratchet is normal to the channel centerline while the other is inclined to the same. When we move from the reservoir, which has DC, applied voltage or the inlet reservoir towards the start of the ratchet geometry, if the direction of first ratchet surface which comes in contact with the fluid, is normal to the center of the microchannel, then it is termed as forward ratchet channel. The forward ratchet channel also has the same dimensions as the symmetric channel discussed before. For the development of numerical model of forward channel, all the parameters are same as the symmetric channel except for the change in shape.

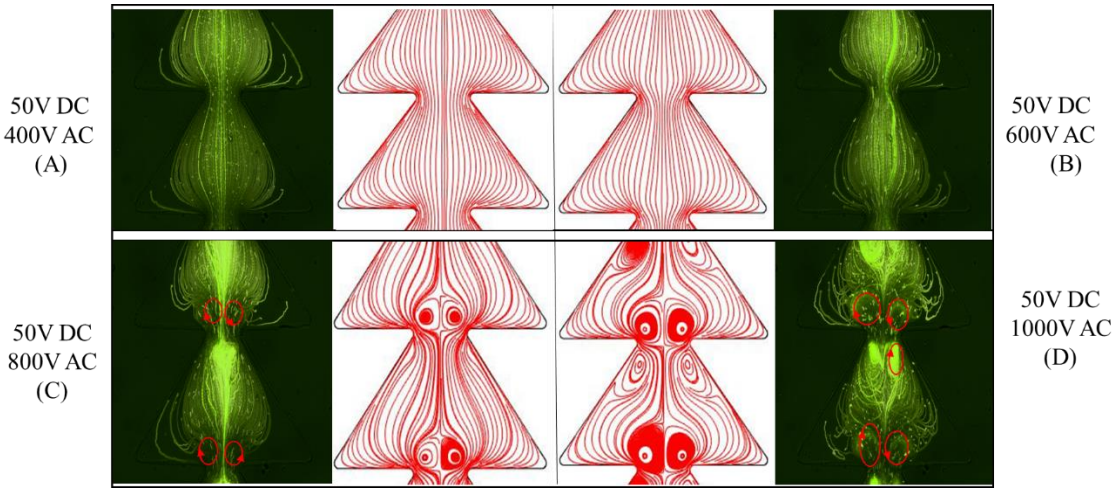

Figure 5.3 shows the comparison between experimentally obtained superimposed images of pathlines for different AC voltages and the numerically predicted image of streamlines for different AC voltages. The development of electrothermal vortices can be seen for 0.5-micron particles with the increasing AC/DC ratio. The arrowed loop in the 50V DC and 1000V AC shows the direction of the electrothermal vortices.

Figure 5.3 shows the comparison between the experimentally obtained superimposed images of pathlines and numerically predicted image of streamlines for a 0.5-micron

particle in asymmetric forward ratchet channel geometry. For the both the experimental and numerical part the AC/DC is increased from 50V DC 400V AC to 50V DC to 1000V AC. For the 50V DC 400V AC and 50V DC 600V AC voltage the streamlines lines does not seem to be effected so we can say that electrothermal flow is not strong enough to overcome to electrokinetic motion. As we further increase the applied voltage to 50V DC 800V AC we can see electrothermal vortices being formed in both the numerical and experimental cases, which implies that electrothermal flow, is now strong enough to overcome local electrokinetic motion. As we further increase the applied voltage to 50V DC 1000V AC the joule heating becomes even stronger and the electrothermal vortices grow in size giving rise to two counter rotating vortices.

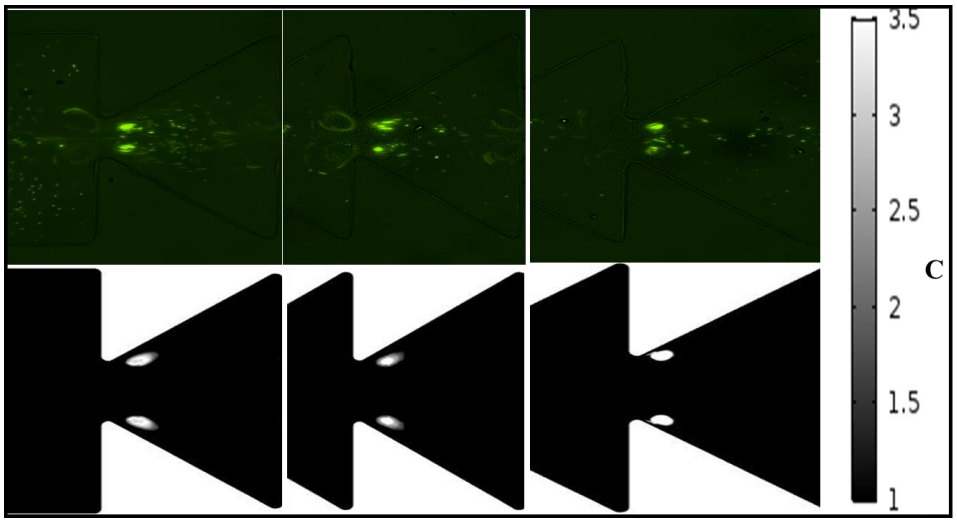

Figure 5.4. Comparison between experimentally obtained images of particle entrainment in the electrothermal vortices and the numerically predicted images of particle entrainment in the vortices for 0.5 micron particle at 20 sec, along the length of the channel.

Figure 5.4. Shows Comparison between experimentally obtained snapshot of particle entrainment in the electrothermal vortices and the numerically predicted images in a forward ratchet channel, for a 0.5mciron particle at 20 sec. Similar to the way of symmetric ratchet channel, we see a decreasing trend in the concentration of particle as we move from outlet of channel to the inlet of the channel. The numerical results seem to be in agreement with the experimental observations. As for the forward channel we changed the shape of the ratchet, the overall effect in the concentration of particle is not significant. A small change in comparison to symmetric channel that we can observe is that the size of the vortex looks a bit elongated which is due to the change in shape of the channel. However, the overall change in concentration is not significant for both the experimental results and the numerically predicted results. After reviving the cases for backward ratchet and forward ratchet, we can say that the change in shape of the channel does not seem to effect the particle entrainment in a significant way.

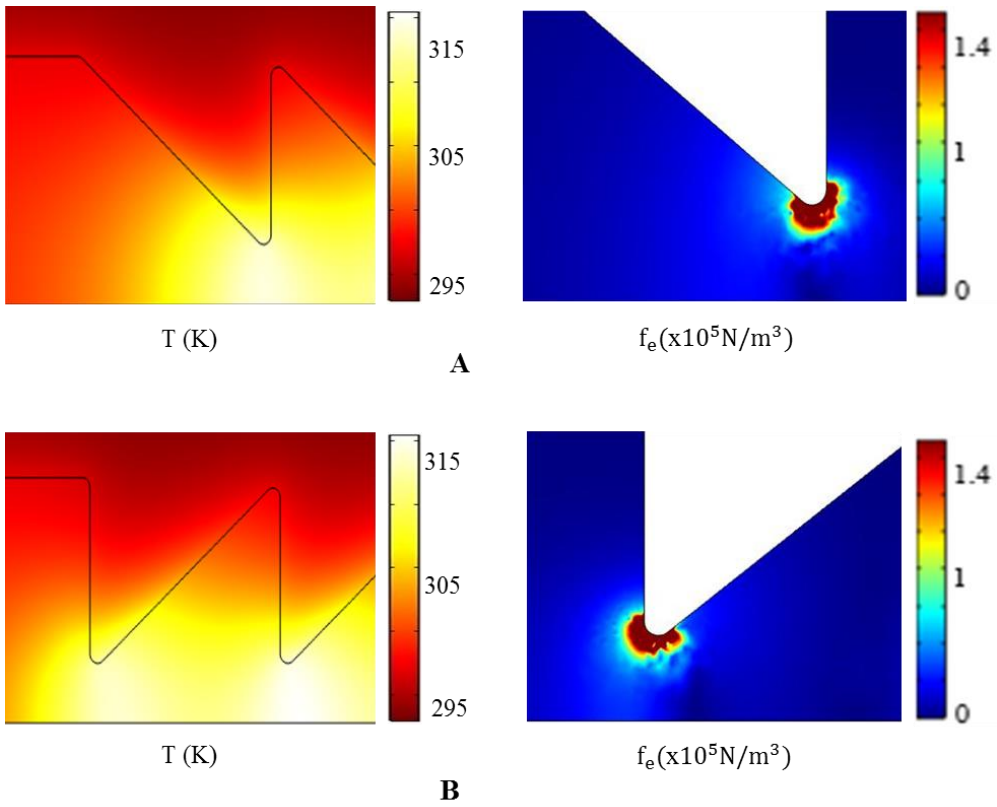

Figure 5.5. (A) Part of the image shows the temperature and electrothermal body force distribution in backward channel while (B) part shows part of the image shows the temperature and electrothermal body force distribution in forward channel.

Figure 5.5 shows a comparison between (A) backward channel and (B) forward channel properties temperature (left side) and electrothermal body force (right side) for a 50V DC and 1000V AC applied voltage. It can be clearly seen from the above figure that the change in the shape of the ratchet channel does not affects the temperature field and the electrothermal body force field. When electric field is applied, it is amplified in the constriction region, which gives rise to joule heating and the temperature rise. The gradients in temperature gives rise to electrothermal body force. These entire phenomenon occur in same way as say in symmetric channel. Since the area of the constriction does not

change with change in the shape of the ratchet, the temperature rise and other fluid properties show the same variation as symmetric channel and hence not repeated here again.

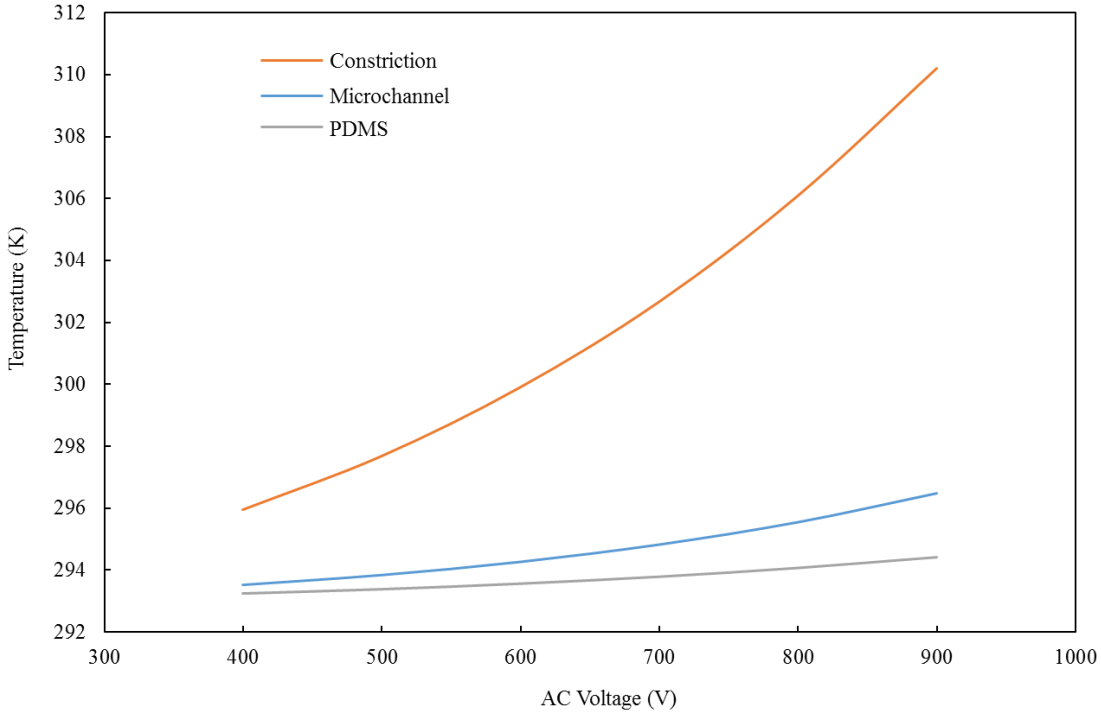

Figure 5.6. Numerically predicted variation of temperature, with the change in AC voltage keeping DC voltage fixed. Graph is plotted for three different locations on computational domain.

When the AC Voltage is increases, the electrothermal fluid circulations grows in size as shown in figure 5.6. This is due to joule heating effect which occurs due to temperature gradients which cause gradients in fluid property. This change in temperature with AC voltage at different locations is plotted in figure 4.3. Different locations are 1. Centre of microchannel 2. Constriction region (5μm below the tip of ratchet) 3. PDMS region (200μm above the constriction in PDMS). The fluid temperature rise with increase in AC

voltage for the constriction region is parabolic in nature. For the microchannel, PDMS region the rise in temperature is very small. This shows that the major heat produced is rejected along the depth wise direction especially through the glass side at the bottom [106,103].

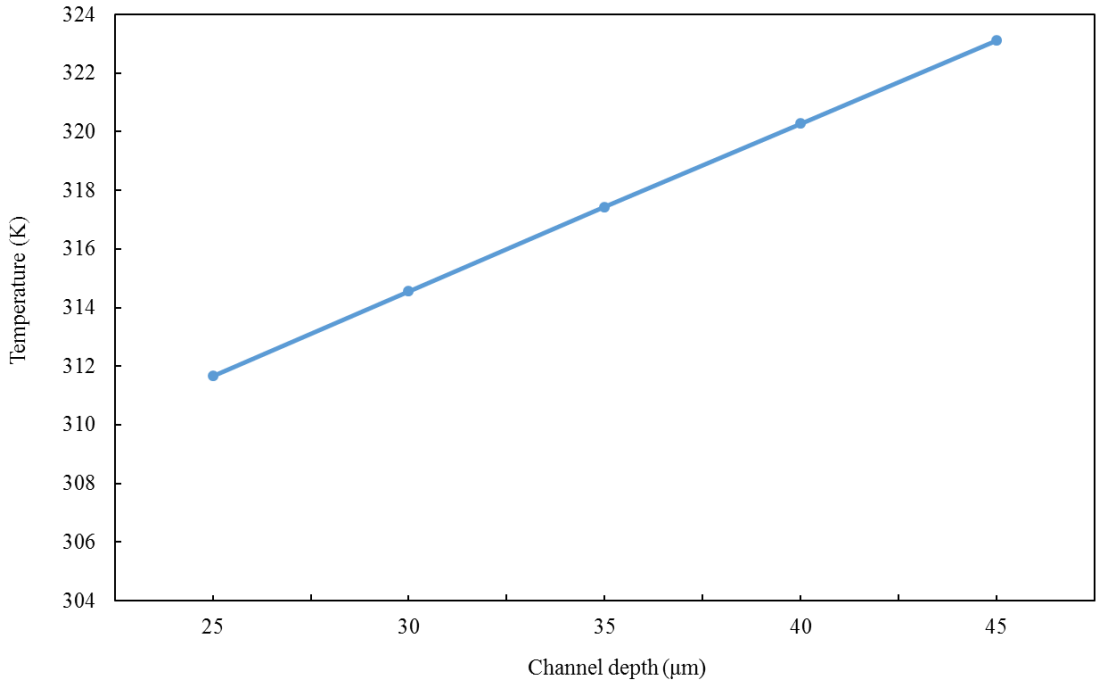

Figure 5.7 shows the variation of temperature with the depth of the channel varying from A. 30 μm B. 35 μm C. 40μm D. 45μm.

The above figure shows the variation of temperature with the depth of channel. The graph for the variation of temperature with the depth of the channel shows a linear variation. As we increase the depth of the channel, the temperature increase linearly. These

results are consistent with what can be predicted by varying the values in final depth average energy equation 3.D.7.

5.4 Summary

In this section, we will summarize all the different results that we investigated in our experimental and numerical analysis. We study the effect of joule heating inside a ratchet channel when electric field is applied across the microchannel. Due to amplification of electric field in ratchet constriction region, electrothermal fluid circulations are formed near the tip of the ratchet. Initially with low ac voltage of 600 V the electrothermal flow is not strong enough to overcome electroosmotic flow but as we increase the AC voltage the electrothermal starts to dominate electroosmotic flow and formation of vortices can be seen near ratchet channel. On increasing the voltage the joule heating increases and electrothermal vortices grow in size. Moreover, in our model we have 0.5 micron particles with uniform concentration initially. After the electrothermal vortices are developed these particles can be seen trapped inside these electrothermal vortices. So the joule heating with the formation of these vortices gives us a medium to trap and manipulate particles. For the numerical part of the modelling, we develop a 2D depth average model, which in comparison to 2D model gives much accurate results and much less computational time as compared to 3D modelling without much deviation from the results. The numerical predicted results are found out to be in good consistency with experimental observations, which validates the modelling. Further we do parametric study by changing the shape of the ratchet, changing the applied voltage and changing the depth of the channel. By changing the shape of the ratchet, the change in electrothermal vortex and particle

entrainment within these vortices is not much affected. No change in temperature and electrothermal body force is observed. Therefore, we can say that by changing the shape of ratchet does not significantly affect the outcome. By changing the applied AC voltage, the joule heating increase and the temperature increases parabolically for constriction region and linearly for other parts of device. As we change the depth of the channel, we observe a linear rise in temperature, which is consistent with the 2D depth equations. In the next and final chapter, we will discuss the conclusion of this thesis work and talk about the possible future work.

CHAPTER SIX

CONCLUSION AND FUTURE WORK

6.1 Conclusion

In this work, we investigate the behavior of electrokinetic flow under the influence of electric field. Joule heating is an inevitable phenomenon that occurs when electric field is passed through a conducting medium, giving rise to electrothermal flows. We use a ratchet channel geometry inside the microchannel, which serves the purpose of constriction region and electrothermal vortices are formed near the ratchet tip. Previously, joule heating had been considered to severely affect the particle manipulation in insulator based dielectrophoretic micodevices. However, in this work we exploit the electrothermal flows caused due to joule heating to actually enhance the sub-micron particle trapping inside the constriction region. The previous work used a semi-transient modelling however, in this work we use a full transient model with depth average modelling which gives us results using much less computational time and resources in comparison to 3D modelling. With a full transient model, we can also investigate the behavior of other variable such as electric field, temperature with change in time. The 2D depth model also serves as very useful tool in giving better accuracy results as compared to 2D model.

Electrokinetics is a preferred way to manipulate particles which are suspended in a fluid. In the first chapter we discuss about the motivation and objective behind the work done in this thesis. Electrokinetics itself is a family of different effects that occur in a fluid and a background detail about electrical double layer, electroosmosis, electrophoresis and

dielectrophoresis is discussed in the first chapter. In our work we exploit the electrothermal flow which occur due to joule heating effect, therefore we discuss joule heating as well. Joule heating is a phenomenon in which the heating of the electrolyte takes place when electric field is made to pass through a constriction region, which is a ratchet channel region in our case. After the introduction of the background details we then move on to discuss details about experimental and numerical work.

In chapter 2, we discuss the experimental methods and process that was performed in the lab by our research group. Image of our experimental setup and schematic of numerical model are compared to better understand the system because our numerical model is developed in two-dimension frame. The experimental results that we obtain after post processing are used to validate out numerical modelling. After discussing about the experimental process, numerical details about the how the modelling is done and the software details are discussed. Since joule heating is a major factor in this work, which occurs due to temperature dependent fluid properties, we also discuss the temperature dependence of fluid properties and various other properties of PDMS, fluid and wall and particle zeta potential.

As mentioned before, we have developed a 2D depth model, which helps us give us results that are as good as 3D modelling results with much less utilization of computational resources, which also makes this modelling automatically better than only 2D modelling. For depth model, we do depth average analysis of the electric field, fluid flow, mass transport and energy equation. We therefore discuss in detail the depth averaging process of these equations. Boundary conditions that are involved with each of the domain is also

discussed. Electric field, fluid flow and mass transport equation are solved for the fluid domain on the model because they are confined in that region. The temperature field is solved for both the fluid and PDMS domain because the heat diffusion takes place starting from the fluid domain towards the outer part of device via conduction and convection. In comparison to experimental work, we only solve for one half of the model because of its symmetric nature, so a symmetry boundary condition is also applied.

In the following two chapters, we compare the experimentally obtained results and numerically predicted results, which validates our modelling. We also perform parametric study to understand the effect on our results when different variables are changed. Since our model is a full transient model, we also study the time development of different fields as well. After electric field is applied, the ratchet constriction region amplifies the electric field which ultimately gives rise to joule heating due to gradient in fluid properties. The variation in electric field along the channel and its development with time is studied. Electric field develops almost instantaneously owing to its confinement in fluid domain and charge relaxation number. Temperature field also varies with the variation of electric field and attains almost steady state after 200ms. The variation in temperature induces gradients in fluid properties, which gives rise to electrothermal flow. At about 50V DC and 800V AC we can see the formation of electrothermal vortices around the ratchet region. This can be validated by comparing with experimental results. On further increasing voltage we can see two counter rotating vortices being formed around ratchet. Development of electrothermal body force, which effects formation of vortices is shown along with other properties such as fluid conductivity, electrical permittivity which also

play role in joule heating. The electrothermal vortices can be further exploited for the entrainment of particles within them. We have an initial uniform concentration of particles throughout the fluid domain. After the formation of vortices, we can see the entrainment of particle within them and an almost four times increase in concertation of particle along with time. However, due to excessive heating that occurs in the model, the experimental work is limited to very short duration of time around twenty seconds. A comparison between the experimentally obtained values of current and numerically predicted values of current is done and the results seem to be consistent with each other with both showing deviation from linear line which shows current variation when joule heating is absent. This further justifies our modelling. Further, in chapter five, we change different parameters and investigate the change in behavior of electrothermal flow. We change the shape of the ratchet channel with backward and forward channel geometry. After analyzing the results and comparing them with the experimentally obtained images, we can say that the shape of the ratchet does not seem to affect the electrothermal flow and particle entrainment at the microchannel region. When we change the applied AC voltage, the joule heating effect increases and the temperature rise across the microdevice can be noted. The depth of channel can also be varied in the numerical model and rise in temperature in a linear fashion is observed which is consistent with the governing equations.

6.2 Future Work

In this work, we investigated the ability of the electrothermal vortices developed due to joule heating to trap sub-micron particles within them. The particle size is small and the conductivity of solution is high which gives rise to joule heating and due to which the

working time of device is very small. In addition, the shape of ratchet does not seem to affect particle entrainment in a significant way. Previous work on the DEP effect [97],where the size of the particle is large and conductivity low and has been neglected here due to much less magnitude as compared to EP, is also an effective way to manipulate particles since it does not generate joule heating and the shape of channel affects the particle manipulation in DEP. We could further develop our work where the size of the particle can be varied in such a way that electrophoresis and dielectrophoresis could both be used to improve the trapping of the particle and increase the working time of the microdevice. A 2D depth model could also be developed which could give us results as good as 3D model with less utilization of resources.

REFERENCES

1. E. K. Sackmann, A. L. Fulton, D. J. Beebe, The present and future role of microfluidics in biomedical research, Nature 507 (2014) 181–189
2. Volpatti, L. R.; Yetisen, A. K. (Jul 2014). "Commercialization of microfluidics devices". Trends in Biotechnology. 32 (7): 347–350.
3. Ryan S. Pawell, David W. Inglis, Tracie J. Barber, and Robert A. Taylor "Manufacturing and wetting low-cost microfluidic cell separation devices"
4. Ghallab, Y.; Badawy, W. (2004-01-01). "Sensing methods for dielectrophoresis Phenomenon: from bulky instruments to lab-on-a-chip"
5. AK Yetisen; L Jiang; J R Cooper; Y Qin; R Palanivelu; Y Zohar (May 2011). "A microsystem-based assay for studying pollen tube guidance in plant reproduction."
6. Samuel K. Sia, George M. Whitesides, Microfluidic devices fabricated in polydimethylsiloxane for biological studies, Electrophoresis 2003, 24, 3563–3576
7. Pratt E D, Huang C, Hawkins B G, Gleghorn J P and Kirby B J 2011,Rare cell capture in microfluidic devices, Chem. Eng.Sci. 66 1508–22
8. Karimi A, Yazai S and Ardekani A M 2013, Hydrodynamic mechanism of cell and particle trapping in microfluidics, Biomicrofluidics 7 021501
9. Wong, P. K., Wang, T., Deval, J. H., Ho, C., Electrokinetics in micro devices for biotechnology applications, IEEE/ASME Transactions on Mechatronics, 2004, 9

10. Chung, A. J., Kim, D., Erickson, D., Lab Chip 2008,Electrokinetic microfluidic devices for rapid, low power drug delivery in autonomous microsystems, 8, 330-338

11. Hilhorst, M. J., Somsen, G. W., de Jong, G. J., Electrophoresis 2001,Capillary electrokinetic separation techniques for profiling of drugs and related products, 22, 2542-2564.

12. Pamme, N., Lab Chip 2006, “Magnetism and microfluidics” 6, 24-38.

13. Gijs, M. A., Lacharme, F., Lehmann, U., Chem. Rev. 2010, Microfluidic applications of magnetic particles for biological analysis and catalysis, 110, 1518-1563.

14. Di Carlo, D., Lab Chip 2009, Inertial microfluidics, 9, 3038-3046.

15. Wang, M. M., Tu, E., Raymond, D. E., Yang, J. M., Zhang, H., Hagen, N., Dees, B., Mercer, E. M., Forster, A. H., Kariv, I., Marchand, P. J., Butler, Nature Biotechnology 2005, 23, 83-87

16. Kim, S. B., Yoon, S. Y., Sung, H. J., Kim, S. S., Anal. Chem 2008, “Resolution of Cross-Type Optical Particle Separation” 80, 2628-2630.

17. Laurell, T., Petersson, F., Nilsson, A., Chem. Soc. Rev. 2007, "Chip integrated Strategies for acoustic separation and manipulation of cells and particles” 36, 492-506.

18. Friend, J., Yeo, L., Rev. Mod. Phys. 2011,” Microfluidics driven via acoustic and ultrsonics” 83, 647-704.

19. Yamada, M., Kasim, V., Nakashima, M., Edahiro, J., Seki, M., Biotechnology and Bioengineering 2004, 88, 489-494.

20. Yamada, M., Seki, M., Anal. Chem 2006," Microfluidic particle sorter employing flow splitting and recombining" 78, 1357-1362.

21. Choi, S., Ku, T., Song, S., Choi, C., Park, J. K., Lab Chip 2011, "Continuous blood cell separation by hydrophoretic filtration" 11, 413-418.

22. Kang, Y., Li, D., Microfluid. Nanofluid. 2009, "Electrokinetics motion of cells and particles in microchannels" 6, 431-460.

23. Srivastava, S. K., Gencoglu, A., Minerick, A. R., Anal. Bioanal. Chem. 2010, 399, 301-321.

24. Jubery, T., Z., Srivastava, S. K., Dutta, P., Electrophoresis 2014 "Dielectrophoretic separation of bioparticles in microdevices: a review", 35, 691-713.

25. A. S. Rathore, Joule heating and determination of temperature in capillary electrophoresis and capillary electrochromatography columns, J. Chromatogr. A 1037 (2004) 431–443.

26. X. Xuan, Joule heating in electrokinetic flow, Electrophoresis 298 (2008) 33-43.

27. B. Cetin, D. Li, Effect of Joule heating on electrokinetic transport, Electrophoresis 29 (2008) 994-1005.

28. M. P. Hughes, Strategies for dielectrophoretic separation in laboratory-on-a-chip systems, Electrophoresis 23 (2002) 2569-2582.

29. P. R. Gascoyne, J. Vykoukal, Particle separation by dielectrophoresis, Electrophoresis 23, (2002) 1973-1983.

30. S. K. Srivastava, A. Gencoglu, A. R. Minerick, DC insulator dielectrophoretic applications in microdevice technology: a review, Anal. Bioanal. Chem. 399 (2011) 301-321.

31. J. Regtmeier, R. Eichhorn, M. Viefhues, L. Bogunovic, D. Anselmetti, Electrodeless dielectrophoresis for bioanalysis: theory, devices and applications, Electrophoresis 32 (2011) 2253-2273

32. B. Cetin, D. Li, Effect of Joule heating on electrokinetic transport, Electrophoresis 29 (2008) 994-1005.

33. M. P. Hughes, Strategies for dielectrophoretic separation in laboratory-on-a-chip systems, Electrophoresis 23 (2002) 2569-2582.

34. P. R. Gascoyne, J. Vykoukal, Particle separation by dielectrophoresis, Electrophoresis 23, (2002) 1973-1983.

35. S. K. Srivastava, A. Gencoglu, A. R. Minerick, DC insulator dielectrophoretic applications in microdevice technology: a review, Anal. Bioanal. Chem. 399 (2011) 301-321.

36. J. Regtmeier, R. Eichhorn, M. Viefhues, L. Bogunovic, D. Anselmetti, Electrodeless dielectrophoresis for bioanalysis: theory, devices and applications, Electrophoresis 32 (2011) 2253-2273.

37. H. Morgan, N. G. Green, AC Electrokinetics: colloids and nanoparticles, Research Studies Press Ltd., England, 2003

38. B. J. Kirby, Micro- and nanoscale fluid mechanics: transport in microfluidic devices, Cambridge University Press, Edinburgh, UK, 2010

39. H. Bruus, Theoretical microfluidics, 2nd ed., MIC – Department of Micro and Nanotechnology, Technical University of Denmark, 2005.

40. J. H. Masliyah, S. Bhattacharjee, Electrokinetic and colloid transport phenomena, John Wiley and Sons Inc., New Jersey, 2006.

41. J. Lyklema, Fundamentals of Interface and Colloid Science, Academic Press, New York 1995.

42. D. Li, Electrokinetics in Microfluidics, Elsevier Academic Press, Burlington, MA, 2004.

43. J. H. Masliyah, Electrokinetic Transport Phenomena, Alberta Department of Energy, Edmonton, 1994.

44. B. J. Kirby, Micro- and nanoscale fluid mechanics: transport in microfluidic devices, Cambridge University Press, Edinburgh, UK, 2010

45. Li, D., Electrokinetics in Microfluidics, Elsevier Academic Press, Burlington, MA, 2004.

46. H. Bruus, Theoretical microfluidics, 2nd ed., MIC – Department of Micro and Nanotechnology, Technical University of Denmark, 2005.

47. H. Morgan, N. G. Green, AC Electrokinetics: colloids and nanoparticles, Research Studies Press Ltd., England, 2003

48. D. Branton, D. Deamer, A. Marziali, H. Bayley, S. A. Benner, T. Butler, M. Di Ventra, S. Garaj, A. Hibbs, X. H. Huang, S. B. Jovanovich, P. S. Krstic, S. Lindsay, X. S. Ling, C. H. Mastrangelo, A. Meller, J. S. Oliver, Y. V. Pershin, J. M. Ramsey, R. Riehn, G. V. Soni, V. Tabard-Cossa, M. Wanunu, M. Wiggin, J. A. Schloss, The potential and challenges of nanopore sequencing, Nat. Biotechnol. 26 (2008) 1146–1153.

49. S. G. Lemay, Nanopore-based biosensors: The interface between ionics and electronics, ACS Nano 3 (2009) 775–779. 132

50. J. Clarke, H. C. Wu, L. Jayasinghe, L. Patel, S. Reid, H. Bayley, Continuous base identification for single-molecule nanopore DNA sequencing, Nat. Nanotechnol. 4 (2009) 265-270.

51. Y. Ai, S. W. Joo, Y. Jiang, X. Xuan, S. Qian, Transient electrophoretic motion of a charged particle through a converging–diverging microchannel: Effect of direct current- dielectrophoretic force, Electrophoresis 30 (2009) 2499–2506.

52. Y. Ai, S. Qian, S. Liu, S. W. Joo, Dielectrophoretic choking phenomenon in a converging-diverging microchannel, Biomicrofluidics 4 (2010) 013201.

53. S. Qian, S. W. Joo, W. Hou, X. Zhao, Electrophoretic motion of a spherical particle with a symmetric nonuniform surface charge distribution in a nanotube, Langmuir 24 (2008) 5332–5340.

54. S. Qian, S. W. Joo, Analysis of self-electrophoretic motion of a spherical particle in a nanotube: Effect of nonuniform surface charge density, Langmuir 24 (2008) 4778–4784.

55. H. Liu, S. Qian, H. H. Bau, The effect of translocating cylindrical particles on the ionic

current through a nanopore, Biophys. J. 92 (2007) 1164–1177.

56. S. Qian, A. Wang, J. K. Afonien, Electrophoretic motion of a spherical particle in a converging–diverging nanotube, J. Colloid Interface Sci. 303 (2006) 579–592.

57. Y. Ai, A. Beskok, D. T. Gauthier, S. W. Joo, S. Qian, DC electrokinetic transport of cylindrical cells in straight microchannels, Biomicrofluidics 3 (2009) 044110.

58. Y. Kang, D. Li, Electrokinetic motion of particles and cells in microchannels, Microfluid Nanofluid 6 (2009) 431–460.

59. S. Chen J. Lillard J, Continuous cell introduction for the analysis of individual cells by capillary electrophoresis, Anal Chem. 73 (2001) 111–118.

60. S. M. Davison K. V. Sharp, Boundary effects on the electrophoretic motion of cylindrical particles: concentrically and eccentrically-positioned particles in a capillary, J Colloid Interf Sci 303 (2006) 288–297.

61. S. M. Davison K. V. Sharp, Transient electrophoretic motion of cylindrical particles in capillaries, Nanosci Microsci Therm 11 (2007) 71–83.

62. S. M. Davison K. V. Sharp, Transient simulations of the electrophoretic motion of a cylindrical particle through a 90° corner, Microfluid Nanofluid 4 (2008) 409–418.

63. M. J. Desai D. W. Armstrong, Separation, identification, and characterization of

microorganisms by capillary electrophoresis, Microbiol Mol Biol Rev 67 (2003)38–51.

64. P. S. Dittrich K. Tachikawa A. Manz, Micro total analysis systems: latest advancements and trends, Anal Chem 78 (2006) 3887–3908.

65. J. Ennis, J. L. Anderson, Boundary effects on electrophoretic motion of spherical particles for thick double layers and low zeta potential, J Colloid Interf Sci 185 (1997) 494–514.

66. G. Oliver, C. Simpson, M. B. Kerby, A. Tripathi, A. Chauhan, Electrophoretic migration of proteins in semidilute polymer solutions, Electrophoresis 29 (2008) 1152–1163.

67. D. S. Reichmuth, S. K. Wang, L. M. Barrett, D. J. Throckmorton, W. Einfeld, A. K. Singh, Rapid microchip-based electrophoretic immunoassays for the detection of swine influenza virus, Lab Chip 8 (2008) 1319–1324.

68. M. A. Rodriguez, D. W. Armstrong, Separation and analysis of colloidal/nanoparticles including microorganisms by capillary electrophoresis: a fundamental review, J Chromatogr B 800 (2004) 7–25.

69. J. G. Shackman, M. S. Munson, D. Ross, Gradient elution moving boundary electrophoresis for high-throughput multiplexed microfluidic devices, Anal Chem 79

(2007) 565–571.

70. A. A. Shugai, S. L. Carnie, Electrophoretic motion of a spherical particle with thick double layer in bounded flows, J Colloid Interf Sci 213 (1999) 298–315.

71. J. N. Stuart, J. V. Sweedler, Single-cell analysis by capillary electrophoresis, Anal Bioanal Chem 375 (2003) 28–29.

72. Z. Wu, Y. Gao, D. Li, Electrophoretic motion of ideally polarizable particles in a microchannel, Electrophoresis 30 (2009) 773-781.

73. X. Xuan, D. Li, Focused electrophoretic motion and selected electrokinetic dispensing of particles and cells in cross-microchannels, Electrophoresis 26 (2005) 3552–3560.

74. X. Xuan, B. Xu, D. Li, Accelerated particle electrophoretic motion and separation in converging–diverging microchannels, Anal Chem 77 (2005) 4323–4328.

75. X. Xuan, C. Ye, D. Li, Near-wall electrophoretic motion of spherical particles in cylindrical capillaries, J Colloid Interf Sci 289 (2005) 286–290.

76. X. Xuan, S. Raghibizadeh, D. Li, Wall effects on electrophoretic motion of spherical polystyrene particles in a rectangular poly(dimethylsiloxane) microchannel, J Colloid Interf Sci 296 (2006) 743–748.

77. E. Yariv, H. Brenner, The electrophoretic mobility of an eccentrically positioned spherical particle in a cylindrical pore, Phys Fluids 14 (2002) 3354–3357.

78. E. Yariv, H. Brenner, The electrophoretic mobility of a closely fitting sphere in a cylindrical pore, SIAM J Appl Math 64 (2003) 423–441.

79. T. Yasukawa, K. Nagamine, Y. Horiguchi, H. Shiku, M. Koide, T. Itayama, F. Shiraishi, T. Matsue, Electrophoretic cell manipulation and electrochemical Genefunction analysis based on a yeast two-hybrid system in a microfluidic device, Anal Chem 80 (2008) 3722–3727.

80. C. Ye, D. Li, Electrophoretic motion of a sphere in a microchannel under the gravitational field, J Colloid Interf Sci 251 (2002) 331–338.

81. C. Ye, D. Li, 3-D transient electrophoretic motion of a spherical particle in a Tshaped rectangular microchannel, J Colloid Interf Sci 272 (2004) 480–488.

82. C. Ye, D. Li, Electrophoretic motion of two spherical particles in a rectangular microchannel, Microfluid Nanofluid 1 (2004) 52–61.

83. C. Ye, D. Sinton, D. Erickson, D. Li, Electrophoretic motion of a circular cylindrical particle in a circular cylindrical microchannel, Langmuir 18 (2002) 9095–9101.

84. C. Ye, X. Xuan, D. Li, Eccentric electrophoretic motion of a sphere in circular

cylindrical microchannels, Microfluid Nanofluid 1 (2005) 234–241.

85. H.A. Pohl, Dielectrophoresis, Cambridge University Press, Cambridge, UK, 1978.

86. H.A. Pohl, The motion and precipitation of suspensoids in divergent electric fields, J. Appl. Phys. 22 (1951) 869–871.

87. Patel, S., Showers, D., Vedantam, P., Tzeng, T., Qian, S., Xuan, X., High throughput particle manipulation by hydrodynamics, Biomicrofluid. 2012, 6, 034102.

88. Patel, S., Qian, S., Xuan, X., Reservoir based dielectrophoresis for microfluidic particle separation by charge, Electrophoresis 2013, 34, 961-968.

89. Regtmeier, J., Eichhorn, R., Viefhues, M., Bogunovic, L., Anselmetti, D., Electrodeless dielectrophoresis for bioanalysis, Electrophoresis 2011, 32, 2253-2273.

90. Jen, C. P., Chen, W. F.,An insulator based dielectrophoretic microdevice for the simultaneous filtration and focusing of biological cell, Biomicrofluidics 2011, 5, 044105.

91. Cetin, B., Li, D., Effect of joule heating in electrokinetic transport, Electrophoresis 2008, 29, 994-1005.

92. Evenhuis, C. J., Haddad, P. R., Joule heating effects and the experimental determination of temperature during CE, Electrophoresis 2009, 30, 897-909.

93. Gonzalez A, Ramos A, Morgan H, Green, N. G., Castellanos, A. C., AC Electric Field induced fluid flow in micro electrodes, J.87 Fluid Mech. 2006, 564, 415-433.

94. A. Sze, D. Erickson, L. Ren, D. Li, Zeta-potential measurement using the Smoluchowski equation and the slope of the current–time relationship in electroosmotic flow, Journal of Colloid and Interface Science 261 (2003) 402–410.

95. Prabhakaran, R.A., Yilong, Z., Patel, S., Kale, A., Song, Y., Hu, G., Xuan, X., "Joule heating effect on electroosmotic entry flow", Electrophoresis 2017, 38, 572-579

96. Sridharan, S., Zhu, J., Hu, G., Xuan, X., Joule heating effect on electroosmotic flow in insulator based dielectrophoresis, Electrophoresis, 2011, 32, 2274-2281.

97. Kale, A., PhD Dissertation, "Joule heating effects in insulator based Dielectrophoresis Microdevices", Clemson University, Clemson SC 2015.

98. Casterllanos, A., Ramos, A., Gonzalez, A., Green, N. G., Morgan, H., J. Phys. D A review of forces in microelectrode structures, Phys. D2003, 36, 2584-2597.

99. R. Pethig, Dielectrophoresis: An assessment of its potential to aid the research and practice of drug discovery and delivery, Advanced Drug Delivery Reviews65(2013) 1589–1599

100. Kale, A., Patel, S., Hu, G., Xuan, X., Numerical modelling of joule heating effect on reservoir based dielectrophoresis, Electrophoresis 2013, 34, 674-683.

101. Kale, A., Patel, S., Qian, S., Hu, G., Xuan, X., Joule heating effect on insulator based dielectrophoresis, Electrophoresis 2014, 35, 721-727.

102. Lin, H., Storey, B. D., Santiago, J. G., A depth average electrokinetic model for shallow microchannel J. Fluid Mech. 2008, 608, 43-70.

103. Green, N. G., Ramos, A., Morgan, H., A survey of sub micrometer particle dynamics J. Phys. D 2000, 33, 632-641.

104. F. Gielen, A.J. deMello, J.B. Edel, Dielectric Cell Response in Highly Conductive Buffers, Anal. Chem. 84 (2012) 1849-1853.

105. S. Sridharan, J. Zhu, G. Hu, X. Xuan, Joule heating effects on electroosmotic flow in insulator-based dielectrophoresis, Electrophoresis 32 (2011) 2274-2281.

106. Erickson, D., Sinton, D., Li, D., Joule heating and heat transfer in poly (dimethylsiloxane) microfluidic system Lab Chip 2003, 3, 141-149.